Technical Report
797

Applications of Mathematical Morphology to Range Imagery

T.R. Esselman
J.G. Verly

23 December 1987

Lincoln Laboratory

MASSACHUSETTS INSTITUTE OF TECHNOLOGY

LEXINGTON, MASSACHUSETTS

ADA189316

This technical report has been reviewed and is approved for publication.

FOR THE COMMANDER

Hugh L. Southall

Hugh L. Southall, Lt. Col., USAF
Chief, ESD Lincoln Laboratory Project Office

MASSACHUSETTS INSTITUTE OF TECHNOLOGY
LINCOLN LABORATORY

APPLICATIONS OF MATHEMATICAL MORPHOLOGY
TO RANGE IMAGERY

T.R. ESSELMAN
J.G. VERLY
Group 21

TECHNICAL REPORT 797

23 DECEMBER 1987

LEXINGTON   MASSACHUSETTS

ABSTRACT

Although little known, mathematical morphology offers great potential in the areas of image enhancement, feature extraction, and object recognition. This work explores this growing field through a survey of established morphological algorithms and the development of new morphological algorithms for range image analysis. With range imagery, mathematical morphology is used for noise removal, 2-D feature extraction, 3-D feature extraction, and 3-D corner extraction.

Contents

List of Figures

Notation

$A, B, T1, T2, X$ subsets of $\mathbf{R}^n$

$\cup$ union

$\cap$ intersection

$\emptyset$ empty set

$[\ ]^c$ complement

x, y, z vectors in $\mathbf{R}^n$

$x \in X$ x is an element of X

$A \subset X$ A is a subset of X

A_x translate of A by vector x

$\{x : P\}$ set of points satisfying property P

Ψ^* dual of set transformation Ψ, i.e.,

$$\Psi^*(A) = [\Psi(A^c)]^c$$

$A \oplus B$ Minkowski addition of sets A and B, i.e.,

$$A \oplus B = \{x + y : x \in A, y \in B\} = \bigcup_{y \in B} A_y$$

$\check{B}$ symmetric set of B, i.e., $\check{B} = \{-x : x \in B\}$

$A \oplus \check{B}$ dilation of A by B

$A \ominus B$ Minkowski difference of sets A and B, i.e.,

$$A \ominus B = \bigcap_{y \in B} A_y$$

$A \ominus \check{B}$ erosion of A by B

A_B opening of A by B, i.e., $A_B = (A \ominus \check{B}) \oplus B$

A^B closing of A by B, i.e., $A^B = (A \oplus \check{B}) \ominus B$

$A \circledast T$ hit-or-miss transformation of A by $T \equiv (T1, T2)$, i.e.,

$$A \circledast (T1, T2) = (A \ominus \check{T}1) \cap (A^c \ominus \check{T}2)$$

f, g	functions defined on $\mathbf{R}^n$
$Ros(f)$	region of support of f (region over which f is defined)
ψ^*	dual of function transformation ψ, i.e.,
	$\psi^*(f) = -\psi(-f)$
$U(f)$	umbra of function f, i.e.,
	$U(f) = \{(x,t) : f(x) \geq t\}, x \in \mathbf{R}^n, t \in \mathbf{R}$
$f \oplus g$	Minkowski addition of functions f and g, i.e.,
	$[f \oplus g](x) = max[f(x-y) + g(y)], y \in Ros(g)$
$\breve{g}(x)$	symmetric function of g, i.e., $\breve{g}(x) = g(-x)$
$f \oplus \breve{g}$	dilation of f by g
$\hat{U}$	reflected umbra $\hat{U} = \{(x,t) : (x,-t) \in U\}$
$f \ominus g$	Minkowksi difference of functions f and g, i.e.,
	$[f \ominus g](x) = min[f(x-y) - g(y)], y \in Ros(g)$
f_g	opening of f by g, i.e., $f_g = (f \ominus \breve{g}) \oplus g$
f^g	closing of f by g, i.e., $f^g = (f \oplus \breve{g}) \ominus g$
$Mes(X)$	Lebesgue measure of set X, i.e., $Mes(X) =$ volume of X
	$(X \in \mathbf{R}^3)$, $Mes(X) =$ area of X $(X \in \mathbf{R}^2)$, etc.
$Pr\{P\}$	probability of event P
nB	$nB = B \oplus B \oplus B \dots n$ times, where $0B = \emptyset$
$/$	set difference, i.e., $A/B = A \cap B^c$
Z	set representing a measuring window
$S(X)$	skeleton of X, i.e., {x: B_x is a disk centered at x and contained in X, but not in any larger disk containing B_x and included in X}
$S^\theta(X)$	conditional bisector of X, i.e.,
	$S^\theta(X) = \bigcup_{n \geq 0}(X \ominus nB)/[(X \ominus (n+1)B) \oplus \theta B]$

$X \bigcirc T$ thinning of X by T, i.e., $X \bigcirc T = X/(X \circledast T)$

$\{T_i\}$ sequence of hit-or-miss SEs, i.e., $\{T_i\} = \{T_1, T_2, \ldots\} = \{(T_1', T_1''), (T_2', T_2''), \ldots\}$

$X \bigcirc \{T_i\}$ sequential thinning of X by $\{T_i\}$, i.e., $X \bigcirc \{T_i\} = (\ldots ((X \bigcirc T_1) \bigcirc T_2) \ldots)$

$\{T_i\}_\infty$ infinite sequence of hit-or-miss SEs

$x \oplus B; X^c$ conditional dilation of x by B, i.e., $x \oplus B; X^c = (x \oplus B) \cap X^c$

$RB_g(f), RB^g(f)$ rolling ball transform of f by g, i.e., $RB_g(f) = f - f_g$, $RB^g(f) = f^g - f$

$K(h)$ global covariance of a set as a function of vector h, i.e., for set X, $K(h) = Mes(X \cap X_{-h})$

$C(h)$ local covariance of a set as a function of vector h, i.e., for set X, $C(h) = Pr\{x, x + h \in X\}$

Chapter 1

Introduction

Enabling a machine to see is very difficult; we do not even understand how we ourselves see. While machines cannot see very well, they are very good at processing numbers. Perhaps this is why modern approaches to machine vision involve much numerical computation. This numerical approach has one major drawback: it can be very slow, so slow in fact that real-time operation can be impossible. Thus, with the present approach to machine vision, one can see a need for fast computer algorithms and architectures.

With this need for fast algorithms and architectures, the development of *parallel* image processing operators becomes attractive; rather than process a large numerical array sequentially, it would be faster to distribute the computational effort across the array, computing the result in parallel. Also, the development of *general* image processing operators is desirable; the use of a few simple operators for many different types of processing would greatly simplify hardware design. As we can see, *general* and *parallel* operators are very appealing for machine vision.

Among the candidates for these *general/parallel* operators, one type stands out: the operators from the field of mathematical morphology. These operators show promise as *general/parallel* image operators, as well as being founded on a solid mathematical basis.

Mathematical morphology (MM) was developed in the mid-1960s by G. Matheron and J. Serra at the Paris School of Mines at Fontainebleau, France. Their intent was to build a solid mathematical foundation for studying the relationship between the geometric and milling properties of ores. Within this context of metallography and petrography, the development of MM algorithms has expanded. However, outside these areas, relatively little has been done to more fully explore the applications of MM. In particular, very few people have applied the techniques of MM to range images, where geometric analysis seems especially appropriate. This work brings to light several applications of MM through a survey of established morphological algorithms. Also, new morphological algorithms for range image analysis are developed.

The organization of this thesis is as follows. Chapter 2 is a tutorial on MM. Chapter 3 is a survey of several established MM algorithms. Chapter 4 explores experiments on real range data while Chapter 5 covers experiments on synthetic range data. The conclusion (Chapter 6) is followed by an extensive bibliography, including comments on many of the references.

Chapter 2

Mathematical Morphology

This chapter presents the basic operations of MM and then some of the special properties relevant to their implementation. Most of the formulas are taken directly out of [26,34] where other details can be found.

2.1 Basic Operations

The basic operations are presented in two subsections. The first corresponds to set MM (used for analyzing signals which can be thought of as sets, such as binary images) and the second to function MM (used for analyzing signals which are thought of as functions, such as gray-scale images).

2.1.1 Set MM

The following notation is used throughout: $A, B, T1, T2$ subsets of $\mathbf{R}^n$; $\cup$ union; $\cap$ intersection; $\emptyset$ empty set; $[\ ]^c$ complement; x, y, z, vectors in $\mathbf{R}^n$; $\{x : P\}$ set of points satisfying property P; Ψ^* dual of set transformation Ψ, i.e., $\Psi^*(A) = [\Psi(A^c)]^c$.

Minkowski Addition and Dilation

The *Minkowski addition* $\oplus$ is defined as $A \oplus B = \{x + y : x \in A, y \in B\}$. One can show that

$$A \oplus B = \bigcup_{y \in B} A_y = \bigcup_{x \in A} B_x, \tag{2.1}$$

where $A_y = A \oplus \{y\}$ is the translate of A by y. The set $\{z : A \cap B_z \neq \emptyset\}$ of the points z such that A hits the translate B_z is called the *dilation* of A by B; the dilation of A by B is also equal to $A \oplus \check{B}$, where $\check{B} = \{-x : x \in B\}$ is the symmetrical set of B with respect to some origin O. For these and all other MM set and function operations the second operand will be referred to as a *structuring element* (SE)[1].

Minkowski Subtraction and Erosion

The dual of $\oplus$ is the *Minkowski subtraction* $\ominus$, i.e., $A \ominus B = (A^c \oplus B)^c$. Using (2.1) and de Morgan's theorem, one finds

$$A \ominus B = \bigcap_{y \in B} A_y. \tag{2.2}$$

Note that, in general, $A \ominus B \neq \bigcap_{x \in A} B_x$. The dual of dilation is *erosion*. The erosion of A by B is the set $\{z : B_z \subset A\}$ of the points z such that the translate B_z is included in A; it is also equal to $A \ominus \check{B}$.

Opening and Closing

By combining the previous operations we obtain the *opening* and *closing*. The opening A_B, and the closing A^B, of A by B are defined as

$$A_B = (A \ominus \check{B}) \oplus B; \qquad A^B = (A \oplus \check{B}) \ominus B. \tag{2.3}$$

From the above equation, it is easy to show that $A_B = ((A^c)^B)^c$, thus, these operations are duals of each other. A_B can be interpreted as the union of all translates of B which are subsets of A. A^B can most easily be interpreted as the dual of the opening.

---

[1]A SE is sometimes referred to as a *kernel*.

Hit-or-miss Transformation

The *hit-or-miss* transformation is defined as

$$A \circledast (T1, T2) = (A \ominus \check{T}1) \cap (A^c \ominus \check{T}2). \tag{2.4}$$

A point z is in $A \circledast (T1, T2)$ if and only if $T1_z$ is a subset of A and $T2_z$ is a subset of A^c. $A \circledast (T1, T2)$ is often denoted $A \circledast T$, where $T \equiv (T1, T2)$ is referred to as a hit-or-miss SE.

Page 13 contains a summary of the basic operations and examples of dilation, erosion, opening, and closing. Example 1 illustrates these four operations in the continuous case while Example 2 shows the corresponding results computed for the discrete case. Note that the dilation and the closing tend to fill in concave corners and indentations; the erosion and the opening tend to cut off convex corners and protrusions. The size of the SE determines which protrusions will be cut off and which indentations will be filled in. Also, note that opening and closing generally preserve the size of the input set, while dilation enlarges the input and erosion shrinks it.

2.1.2 Function MM

The notation is: f, g functions defined on $\mathbf{R}^n$; x, y vectors in $\mathbf{R}^n$; $Ros(f)$ region of support of f (region over which f is defined); ψ^* dual of function transformation ψ, i.e., $\psi^*(f) = -\psi(-f)$.

The *umbra* U of a function f is

$$U(f) = \{(x, t) : f(x) \geq t\} \qquad x \in \mathbf{R}^n \qquad t \in \mathbf{R}. \tag{2.5}$$

The correspondence between a function and its umbra is unique, thus we can define MM function operations in terms of MM set operations on the umbras.

EXAMPLE 2

1. ORIGINAL 2. SE 3. DILATION 4. EROSION 5. CLOSING 6. OPENING

Set MM tutorial.

OPERATIONS

- **MINKOWSKI ADDITION:** $A \oplus B = \{a + b : a \in A, b \in B\}$

$$= \bigcup_{x \in B} A_x = \bigcup_{y \in A} B_y$$

- **MINKOWSKI SUBTRACTION:** $A \ominus B = (A^c \oplus B)^c = \bigcap_{x \in B} A_x$ WHERE $\check{B} = \{-x : x \in B\}$

- **DILATION:** $\{z : A \cap B_z \neq \emptyset\} = A \oplus \check{B}$
- **EROSION:** $\{z : B_z \subset A\} = A \ominus \check{B}$
- **CLOSING:** $A^B = (A \oplus \check{B}) \ominus B$
- **OPENING:** $A_B = (A \ominus \check{B}) \oplus B$
- **HIT-OR-MISS TRANSFORMATION:**

$$A \circledast (T1, T2) = (A \ominus \check{T}1) \cap (A^c \ominus \check{T}2)$$

EXAMPLE 1

DILATION $A \oplus \check{B}$

EROSION $A \ominus \check{B}$

OPENING A_B

CLOSING A^B

13
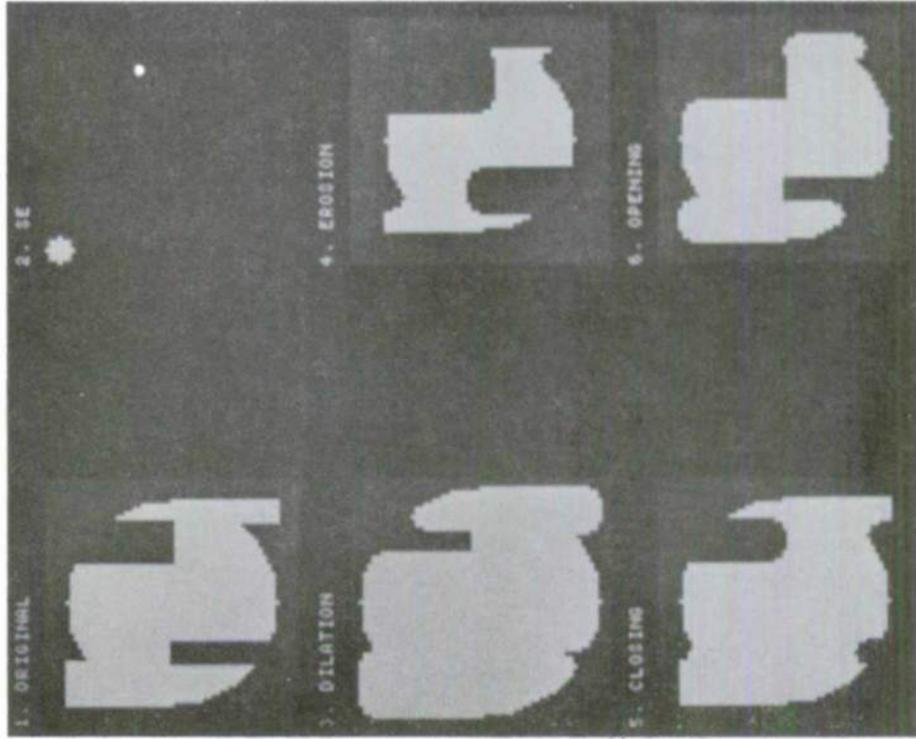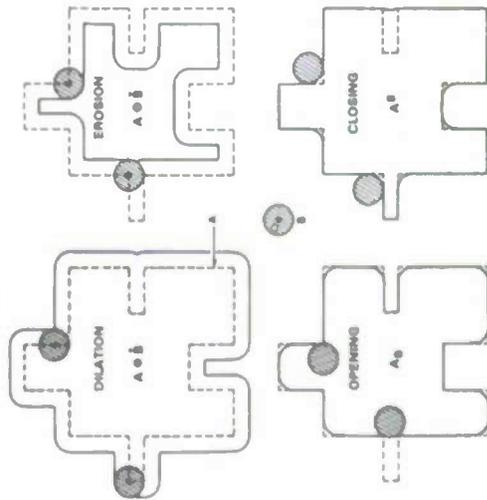
Minkowski Addition and Dilation

The Minkowski addition of f and g is defined through

$$f \oplus g \to U(f \oplus g) = U(f) \oplus U(g), \tag{2.6}$$

where the arrow indicates the correspondence to the umbra of the result. Dilation of f by g is

$$f \oplus \breve{g} \to U(f \oplus \breve{g}) = U(f) \oplus U(\breve{g}), \tag{2.7}$$

where $\breve{g}(x) = g(-x)$.

Minkowski Subtraction and Erosion

The Minkowski subtraction of f and g is defined through $f \ominus g \to U(f \ominus g)$. The right hand side of this expression *cannot* be written as $U(f) \ominus U(g)$ because $U(g)$ extends to $-\infty$ and, according to Equation 2.2, this would reduce the result to a point at $-\infty$. However, since $\oplus$ and $\ominus$ are, by definition, dual operations, we have $f \ominus g = -[(-f) \oplus g]$. Before continuing, we must introduce the reflected umbra $\hat{U} = \{(x,t) : (x, -t) \in U\}$ and two of its properties

$$\hat{U}(f) = [U(-f)]^c \tag{2.8}$$

$$[U(f) \widehat{\oplus} U(g)] = \hat{U}(f) \oplus \hat{U}(g), \tag{2.9}$$

which can be easily established. Thus,[2]

$$
\begin{aligned}
U(f \ominus g) &= U[-((-f) \oplus g)] &&= [\hat{U}((-f) \oplus g)]^c \\
&= [[U(-f) \widehat{\oplus} U(g)]]^c &&= [\hat{U}(-f) \oplus \hat{U}(g)]^c \\
&= [[U(f)]^c \oplus \hat{U}(g)]^c &&= U(f) \ominus \hat{U}(g),
\end{aligned}
$$

i.e.,

$$f \ominus g \to U(f \ominus g) = U(f) \ominus \hat{U}(g). \tag{2.10}$$

Erosion of f by g is

$$f \ominus \breve{g} \to U(f \ominus \breve{g}) = U(f) \ominus \hat{U}(\breve{g}). \tag{2.11}$$

---

[2]This derivation is somewhat more direct than that given in [34].

Opening and Closing

The opening f_g and closing f^g of f by g are defined as

$$f_g = (f \ominus \breve{g}) \oplus g; \qquad f^g = (f \oplus \breve{g}) \ominus g. \qquad (2.12)$$

Relations (2.6) and (2.10) can be expressed algebraically as

$$[f \oplus g](x) \quad = max[f(x - y) + g(y)] \qquad y \in Ros(g) \qquad (2.13)$$

$$[f \ominus g](x) \quad = min[f(x - y) - g(y)] \qquad y \in Ros(g), \qquad (2.14)$$

where, by convention, $f = -\infty$ outside $Ros(f)$. Dilation and erosion are given by

$$[f \oplus \breve{g}](x) \quad = max[f(x + y) + g(y)] \qquad y \in Ros(g) \qquad (2.15)$$

$$[f \ominus \breve{g}](x) \quad = min[f(x + y) - g(y)] \qquad y \in Ros(g). \qquad (2.16)$$

This leads to relatively simple algorithms for computation of the function MM operations. Note that (2.13), (2.14), (2.15), and (2.16) are the morphological equivalents of the standard convolution and correlation.

Page 16 contains a summary of the basic operations and examples of dilation, erosion, closing, and opening. Example 1 illustrates these four operations in the continuous, 1-D case while Example 2 shows the corresponding results computed for the discrete, 2-D case. As with set MM, the dilation and the closing tend to fill in concave corners and indentations; the erosion and the opening tend to cut off convex corners and protrusions. The size of the SE determines which protrusions will be cut off and which indentations will be filled in. Also, note that opening and closing generally preserve the size (height and region of support) of the input function, while dilation enlarges the input and erosion shrinks it.

EXAMPLE 2 (2-D)

1. ORIGINAL 2. SE 3. DILATION 4. EROSION 5. CLOSING 6. OPENING

OPERATIONS

RELATED TO SET MM THROUGH THE UMBRA

$$U(f) = \{(x,t) : f(x) \geq t \mid x \in R^n \quad t \subset R$$

- **MINKOWSKI ADDITION:** $f \oplus g \rightarrow U(f \oplus g) = U(f) \oplus U(g)$

- **MINKOWSKI SUBTRACTION:** $f \ominus g \rightarrow U(f \ominus g) = U(f) \ominus \hat{U}(g)$

  $$\text{WHERE } \hat{U} = \{(x,t) : (x,-t) \in U\}$$

- **DILATION:** $\max_{y \in R^n} [f(y) + g(y - x)] = [f \oplus \check{g}](x)$

  $$\text{WHERE } \check{g}(x) = g(-x)$$

- **EROSION:** $\min_{y \in R^n} [f(y) - g(y - x)] = [f \ominus \check{g}](x)$

- **CLOSING:** $f^g = (f \oplus \check{g}) \ominus g$

- **OPENING:** $f_g = (f \ominus \check{g}) \oplus g$

EXAMPLE 1 (1-D)

DILATION $f \odot \check{g}$ EROSION $f \odot \check{g}$

OPENING f_g CLOSING f^g

Function MM tutorial.

16
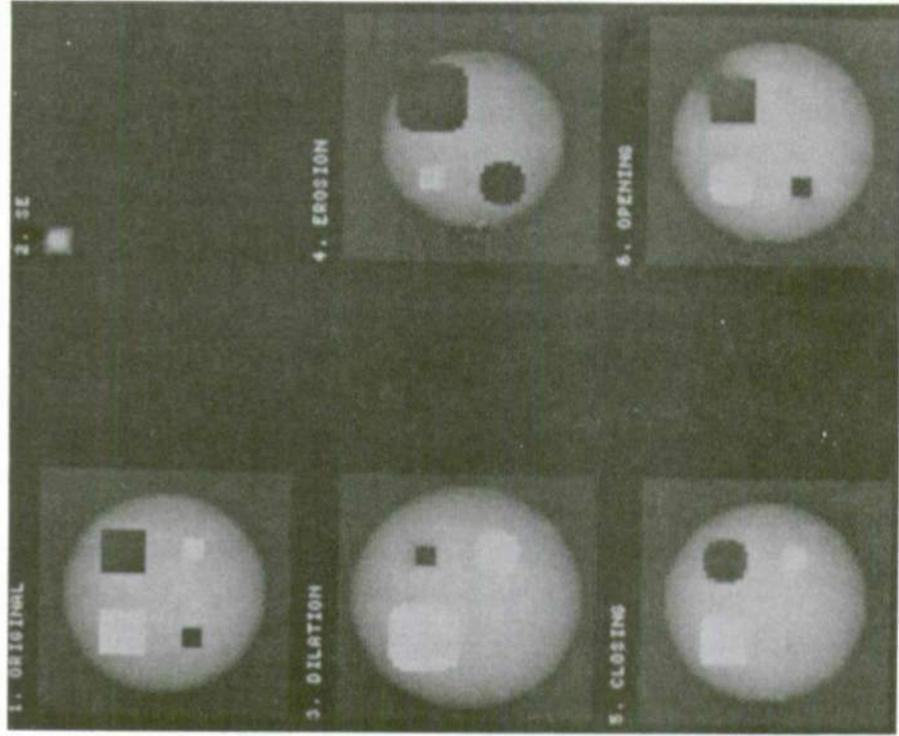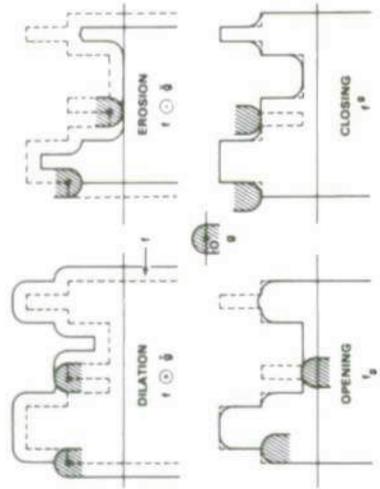
2.2 Properties Relevant to Implementation

This section covers three of the important properties of Minkowski addition and subtraction related to the implementation of the basic MM operations.

The *distributivity* property is

$$A \oplus (B_1 \cup B_2) = (A \oplus B_1) \cup (A \oplus B_2) \tag{2.17}$$

$$A \ominus (B_1 \cup B_2) = (A \ominus B_1) \cap (A \ominus B_2). \tag{2.18}$$

This property implies that one can dilate or erode A by taking $(B_1 \cup B_2)$ piece by piece and then combining the intermediate results by union or intersection. This property also applies to functions, i.e.,

$$f \oplus max(g_1, g_2) = max(f \oplus g_1, f \oplus g_2) \tag{2.19}$$

$$f \ominus max(g_1, g_2) = min(f \ominus g_1, f \ominus g_2). \tag{2.20}$$

The *iterativity* property is

$$A \oplus (B_1 \oplus B_2) = (A \oplus B_1) \oplus B_2 \tag{2.21}$$

$$A \ominus (B_1 \oplus B_2) = (A \ominus B_1) \ominus B_2. \tag{2.22}$$

This property, which applies to functions as well, implies that one can decompose a SE into a Minkowski sum of simpler SEs and then iterate the dilation or erosion to get the intended result. This decomposition property is particularly important to the implementation of morphological operators on cellular logic arrays such as the GLOPR, CLIP, or Cytocomputer (see [53] for a comparison of these computers) which can access only a local neighborhood of pixels, such as a 3×3 window. Zhuang and Haralick [46] have shown how to optimally decompose set MM SEs through a tree search of possible decompositions.

The property of Minkowski addition and subtraction which leads to the fastest implementation, however, comes from the following expressions for these operations.

17

Recall that for sets

$$A \oplus B = \bigcup_{y \in B} A_y$$

$$A \ominus B = \bigcap_{y \in B} A_y$$

and for functions

$$[f \oplus g](x) = max[f(x - y) + g(y)] \qquad y \in Ros(g)$$

$$[f \ominus g](x) = min[f(x - y) - g(y)] \qquad y \in Ros(g).$$

This implies that in the set MM case, the morphological results can be computed as logical combinations of shifted versions of the input image. In the function MM case, the morphological results can be computed by shifting an input image, adding or subtracting a SE value from the shifted image, and then taking the max or min of this and the accumulated result.

2.3   Implementation

For this work, both erosion and dilation[3] have been implemented (for sets and functions) as the basic MM operations; all others such as Minkowski subtraction, Minkowski addition, opening, closing, etc., are implemented as combinations of these basic operations. All operations have been programmed in LISP and C under the SKETCH [69] image understanding operating system developed at the MIT Lincoln Laboratory. This tool was used for all experiments described in Chapters 4 and 5.

---

[3]Dilation can be implemented as the complement of the erosion of the complement (duality).

Chapter 3

Previous Work

This chapter discusses MM algorithms developed through traditional applications of MM. These applications include texture analysis, defect detection, image coding, and biological cell analysis. Throughout the next several sections the discussion will be geared toward the development of an intuitive understanding of MM algorithms, rather than the more rigorous presentation found in [26,34]. The first sections discuss techniques used in the processing of range imagery in Chapters 4 and 5. The last few sections (morphological size and shape description, edge detection and perimeter estimation, and covariance) explore several other useful algorithms which are, however, not used in later chapters.

The notation is: $Mes(X)$ Lebesgue measure of set X, i.e., $Mes(X) =$ volume of X ($X \in \mathbf{R}^3$), $Mes(X) =$ area of X ($X \in \mathbf{R}^2$), etc; $Pr\{P\}$ probability of event P; $nB = B \oplus B \oplus B \ldots n$ times[1] ; / set difference, i.e., $A/B = A \cap B^c$; Z set representing a measuring window.

[1] $0B = \emptyset, 1B = B, 2B = B \oplus B \ldots$
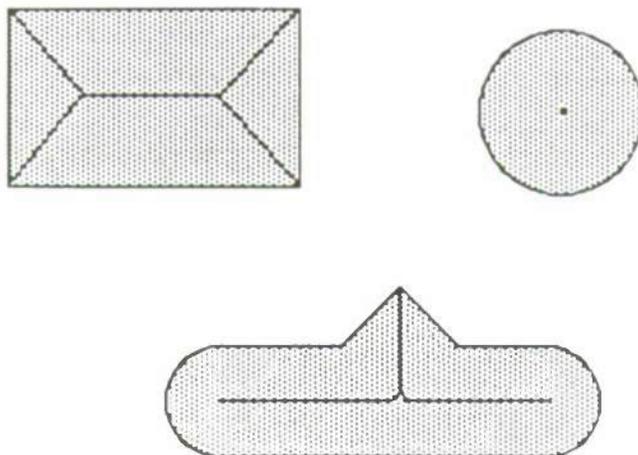
Figure 3.1.   Skeletons.

3.1   Skeleton, Thinning, and Conditional Bisector

3.1.1   Skeleton

A point x is part of the *skeleton* of the set X if the following condition is satisfied:

- If B_x is a disk centered at x and contained in X, there is no larger disk containing B_x and included in X.

The set B_x is called a *maximum disk* and it is the center of each of these maximum disks which make up the skeleton. Examples of skeletons are shown in Figure 3.1. The skeleton can be computed in the following way. If B is the smallest disk on the image grid (Fig. 3.2), the skeleton[2] $S(X)$ is given ([34] p. 389) by

$$S(X) = \bigcup_{n \geq 0} s_n(X) \qquad n \text{ integer} \tag{3.1}$$

$$s_n(X) = (X \ominus nB)/(X \ominus nB)_B. \tag{3.2}$$

The original set X can be reconstructed from the skeleton subsets $s_n(X)$ as follows:

---

[2]The skeleton is virtually identical to the medial axis transform [60,34]. See [34] for a more thorough treatment.

Figure 3.2.   Smallest disk on the square grid.

$$X = \bigcup_n (s_n(X) \oplus nB). \tag{3.3}$$

The capability of representing binary images as skeletons (along with the associated disk size for each skeleton subset) provides for efficient coding of binary images [25].

3.1.2   Thinning

Another transformation which is similar to the skeleton is the *homotopic sequential thinning*.

Thinning, denoted $\bigcirc$, is an application of the hit-or-miss transformation and is defined for $T = (T', T'')$ ([34] p. 390) as

$$X \bigcirc T = X/(X \circledast T). \tag{3.4}$$

An example is shown in Figure 3.3 where T' appears in black and T'' in white within the 3×3 neighborhood. The origins of both T' and T'' are at the center of the 3×3 neighborhood and points of the 3×3 neighborhood which belong to neither T' nor T'' are marked with dots. This pictorial representation (of hit-or-miss SEs used for thinning) will be used throughout the rest of this work.

Sequential thinning involves thinning by a sequence

$$\{T_i\} = \{T_1, T_2, \ldots\} = \{(T_1', T_1''), (T_2', T_2''), \ldots\}$$

of hit-or-miss SEs. The sequential thinning of X by the sequence $\{T_i\}$ is defined as

$$X \bigcirc \{T_i\} = (\ldots((X \bigcirc T_1) \bigcirc T_2)\ldots). \tag{3.5}$$

If the sequence $\{T_i\}$ is infinite (denoted $\{T_i\}_\infty$), the input X is typically thinned until there is no change from one iteration to the next.

21

X

$T = (T', T'')$

X ◯ T
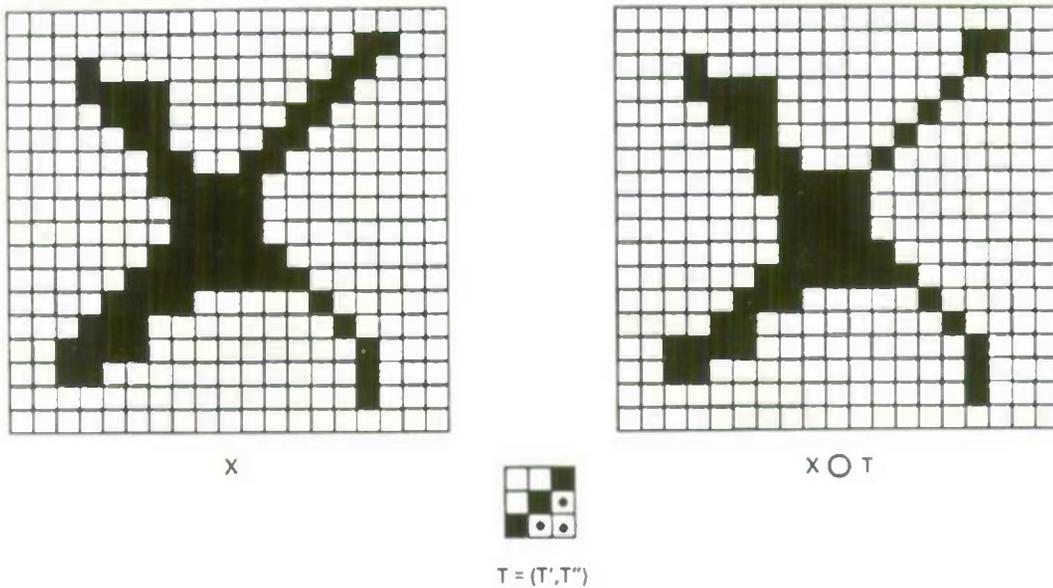
Figure 3.3.   Thinning.

Homotopic thinning is a special case of thinning. To describe what is meant by homotopic, first consider the homotopy tree associated with the set X shown in Figure 3.4 (shaded region). The root of this tree corresponds to the background X_0 (i.e., the infinite connected component of X^c); the first branches correspond to the connected components, X_1 and X_1', of X adjacent to X_0; the second branches correspond to the holes of X_1, adjacent to X_1, etc. A transformation is said to be homotopic if it does not modify the homotopy tree of the input set X. Thus, there is a one-to-one correspondence between connected components of X and the connected components of the homotopic thinning of X.

Homotopic sequential thinning is sequential thinning with a homotopy-preserving SE sequence. An example of such a sequence is the set of consecutive 90-degree rotations of the Levialdi [63] letters L and L' shown in Figure 3.5. Sequential thinning of the set X by the sequence $\{L\}_\infty$ (Fig. 3.5) results in a thin line drawing of X. The result is a kind of "skeleton", although in this case the homotopy of X is preserved. An example is shown in Figure 3.6.

22
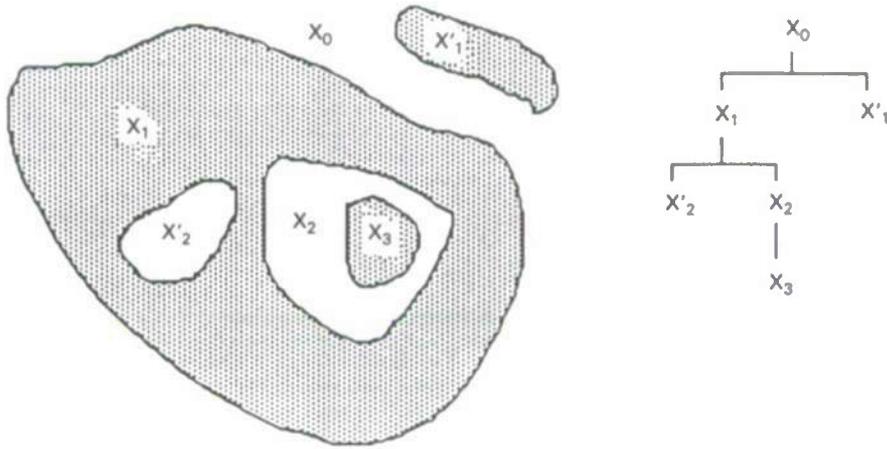
Figure 3.4.   A set and its homotopy tree.
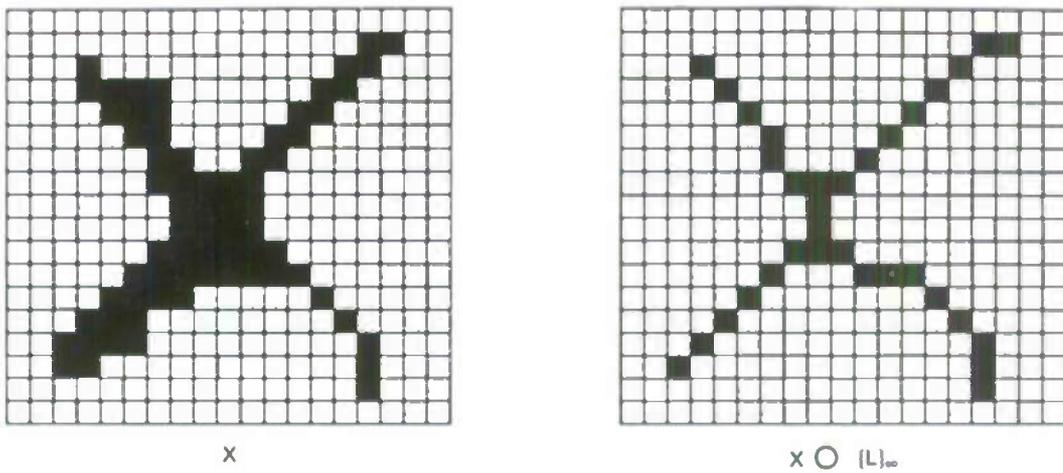

Figure 3.5. $\{L\}_\infty$.

Figure 3.6.   Homotopic sequential thinning.

The homotopic sequential thinning, in combination with the hit-or-miss transformation, can be useful in detecting certain types of defects [28,20]. For example, Mandeville [20] has used the homotopic sequential thinning of printed circuit board images to detect pixel patterns which indicate circuit defects.

3.1.3 Conditional Bisector

The conditional bisector is a subset of the skeleton and is given by the following formula ([34] p. 390, [31]):

$$
\begin{aligned}
S^\theta(X) &= \bigcup_{n \geq 0} (X \ominus nB)/[(X \ominus (n+1)B) \oplus \theta B] \\
&= \bigcup_{n \geq 0} (X \ominus nB)/[(X \ominus nB)_B \oplus (\theta - 1)B], \quad (3.6)
\end{aligned}
$$

where θ is an integer and B is the smallest disk of the grid. Note that the denominator of the second expression is derived from the first as follows:

$$
\begin{aligned}
(X \ominus (n+1)B) \oplus \theta B &= (X \ominus (nB \oplus B)) \oplus (B \oplus (\theta - 1)B) \\
&= (((X \ominus nB) \ominus B) \oplus B) \oplus (\theta - 1)B \\
&= (X \ominus nB)_B \oplus (\theta - 1)B.
\end{aligned}
$$

When θ is one, the conditional bisector is just the skeleton.

One interpretation of the conditional bisector is the part of the set $(X \ominus nB)$ not reached by the set $(X \ominus (n+1)B) \oplus \theta B$. If $(X \ominus (n+1)B) = \emptyset$, then the *ultimate erosion* has been found. The ultimate erosion of X is the erosion by the largest disk nB such that $X \ominus nB \neq \emptyset$. Meyer [31,28] has used this property of the conditional bisector (along with the thinning and the hit-or-miss transformation) for detecting overlapping or non-convex biological cells. A pictorial representation of the algorithm is shown in Figure 3.7.

ORIGINAL SETS   SET DIFFERENCE OF   THINNINGS
ORIGINAL SETS AND
CONDITIONAL BISECTORS
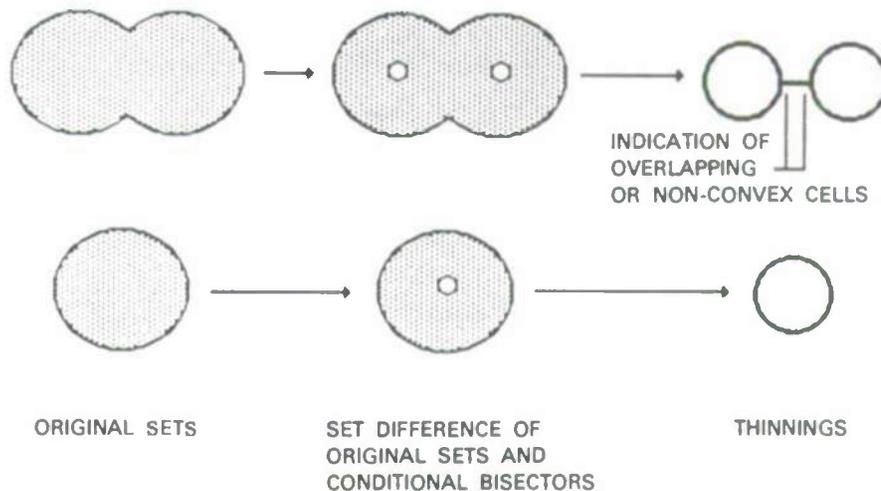
Figure 3.7. Application of the conditional bisector.

3.2 Region Painting, Labelling, and Extraction

Given the boundary X of a region (e.g. a one-pixel wide closed curve) and a single point x of the interior, we can use MM to fill in the region [22]. The first step in "painting" the region consists of dilating the interior point x by the smallest disk B of the grid. Then this result is intersected with the complement, X^c, of the boundary X. This operation of restricting the dilation to a certain region is called conditional dilation and is denoted $x \oplus B; X^c$ ([34] p. 393)[3] . That is,

$$x \oplus B; X^c = (x \oplus B) \cap X^c. \tag{3.7}$$

The next step toward painting the region is to use the results of the first conditional dilation as input to the next conditional dilation. This process is iterated until the region is filled.

Conditional dilation by a sequence can also be used for region labelling and extraction ([34] p. 405). If an input set X consists of several disjoint regions X_i, i.e., $X = \bigcup_i X_i$, we can extract and label the X_i using the following algorithm:

---

[3]The concept of a conditional operation can also be extended to erosion, thinning, closing, etc.
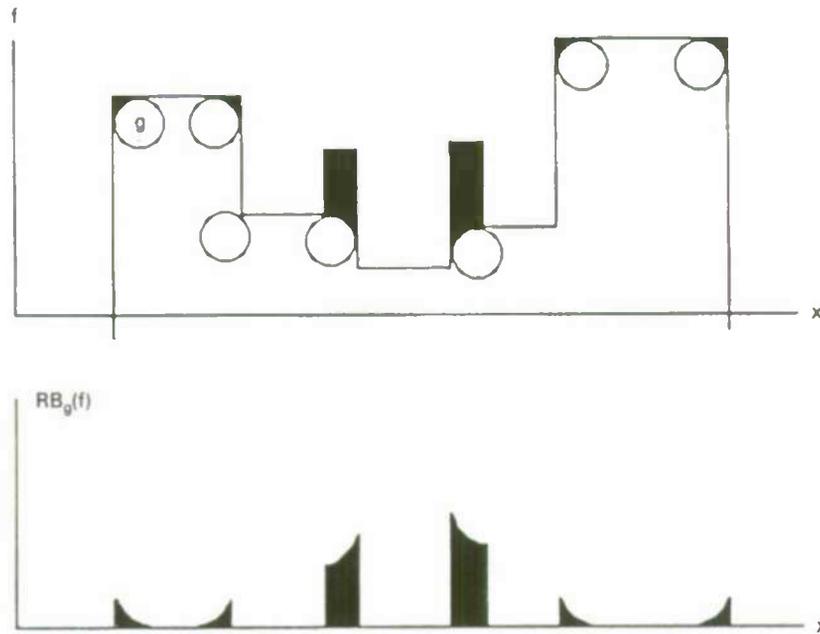
Figure 3.8.   Rolling ball transform (1-D).

1. Scan the input image and stop at the first point $x_i \in X$ ($i = 1$ initially). $X_i = x_i$.

2. $X_i = X_i \oplus B; X$.

3. If step 2 produced no change in X_i, go to 4, else go to 2. This fills in the X_i.

4. $X = X/X_i$, $i = i + 1$, go to 1. This subtracts out the previously labelled X_i.

3.3   Rolling Ball Transform

The *rolling ball transform* [40] is applied primarily to functions although the same idea can be extended to sets. If g is a hemispherical function, the opening f_g is a function defining the places where the hemisphere fits *beneath* the surface of f. The rolling ball transform $RB_g(f) = f - f_g$ then gives all the regions where the hemisphere g does *not* fit beneath the surface of f. This is illustrated in Figure 3.8 for a 1-D function. If the

26

hemisphere g is inverted and moved *above* the function f, the rolling ball transform is denoted $RB^g(f)$ and is equal to $f^g - f$.[4]

One application of the rolling ball transform is background normalization. Sternberg [40] has used it for this purpose on images of human cells.

3.4   Morphological Size and Shape Description

The material in this and the next sections is not exploited in Chapters 4 and 5 but is included because of its importance in the classical applications of MM. Two MM techniques which extract size and shape information are *linear erosion* and the opening with a disk (or sphere in 3-D).

The linear erosion ([34] p. 323) involves eroding the input set X by a segment of length l in direction α, $B(l, \alpha)$. One can obtain a size distribution for a fixed direction α_0 by

$$Mes(X \ominus \check{B}(l, \alpha_0)) \qquad \text{where } l = l_0, l_1, \ldots \tag{3.8}$$

The size and shape distribution can also be measured using the opening of the input by nB, a disk of radius n. By varying the radius n and taking the difference between consecutive openings, the size and shape distribution can be measured, i.e.,

$$Mes(X_{nB}) - Mes(X_{(n+1)B}). \tag{3.9}$$

Examples of size and shape distributions (differences between consecutive openings) are shown in Figure 3.9. Maragos [24] has used the differences between consecutive openings and the dual notion of differences between consecutive closings in defining the *pattern spectrum* of a binary image.

Both linear erosion and opening by disks have probabilistic versions ([34] p. 360). The primary difference is that the measurements described above are divided by the

---

[4]Since there is no standard notation for the rolling ball transform, $RB_g(f)$ and $RB^g(f)$ were arbitrarily selected.
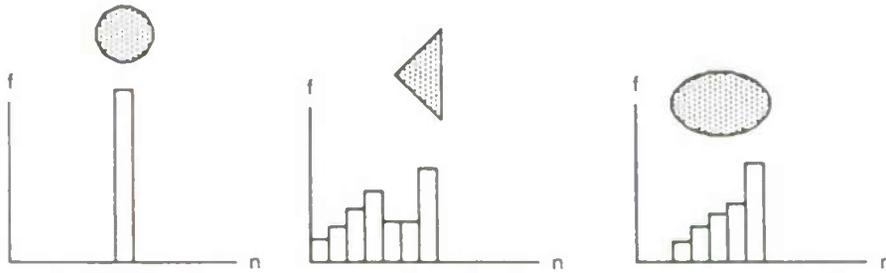
Figure 3.9.   Size and shape distributions as a function of disk size n.

total number of occurences (in the measuring window) of the particular segment or disk. For example, for linear erosion measurements within the window Z, Equation 3.8 becomes

$$\frac{Mes(X \ominus \check{B}(l, \alpha))}{Mes(Z \ominus \check{B}(l, \alpha))}.$$ (3.10)

3.5   Edge Detection and Perimeter Estimation

Minkowski addition and subtraction can be used to locate edges in an image. For a sufficiently small disk, B, of radius r, the edges of a set X are given by

$$(X \oplus B)/(X \ominus B).$$ (3.11)

The perimeter, $U(X)$, of X can also be computed using Minkowski addition and is approximately equal to

$$Mes((X \oplus B)/X).$$ (3.12)

To see this, remember that the Minkowski addition of a small disk and the set X has the effect of "growing" a new layer of "skin" on X. Taking the difference between this new set and the original leaves only the "skin", the measure of which is approximately equal to the perimeter.

Equations 3.11 and 3.12 can be extended to functions for surface area estimation and gray-scale edge detection by using a hemispherical function as the SE.

28

3.6 Covariance

Most of the MM techniques available in the literature have come about through work on texture analysis. One of the most useful techniques for this purpose is what Serra ([34] p. 271) calls the *covariance*. The covariance is useful for

- extracting periodicities from what may seem to be a uniform texture

- analyzing the superposition of scales in an image

- detecting anisotropies at a given scale

The following subsections discuss both the *global covariance* and the *point covariance* (which is a probabilistic version of the global covariance), and an application of each.

3.6.1 Global Covariance

If B is the SE consisting of two points $\{0, h\}$ (h is a vector with magnitude $|h|$ and direction α), the global covariance $K(h)$, defined as $Mes\{x : x, x + h \in X\}$, is given by

$$K(h) = Mes(X \ominus \check{B}) = Mes(X \cap X_{-h}).\qquad(3.13)$$

If $k(x)$ is the characteristic function associated with the set X, the covariance can also be viewed as

$$K(h) = \int_{\mathbf{R}^n} k(x)k(x + h)dx.\qquad(3.14)$$

The following are several properties of $K(h)$: $K(0) = Mes(X)$; $K(h) = K(-h)$; $K(0) \geq K(h)$. An example of global covariance computation can be seen in Figure 3.10.

In most practical situations $K'(0) = \lim_{|h| \to 0} -(K(0) - K(h))/|h|$ exists and it is equal to the *total projection area* ($X \in \mathbf{R}^3$) or *total projection diameter* ($X \in \mathbf{R}^2$) of X in direction α. An example of the total projection diameter is illustrated in Figure 3.11 where it is equal to $\sum_i d_i$.
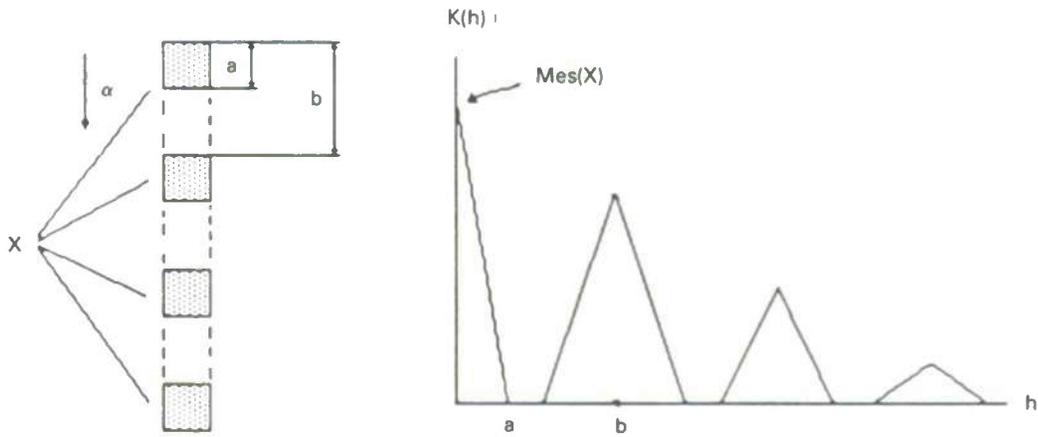
*Figure 3.10.   Global covariance (adapted from [34]).*
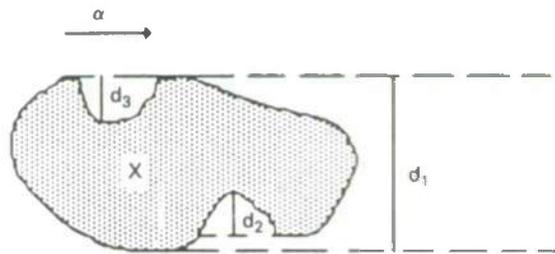
Figure 3.11.   Total diameter of X ($\sum_i d_i$).

30

3.6.2 Point Covariance

If one can observe the set X only within a limited window Z, the *point covariance* $C(h)$, defined as $Pr\{x, x + h \in X\}$, may be a more suitable measure than the global covariance $Mes\{x : x, x + h \in X\}$. A good estimate ([34] p. 281) of $C(h)$ is $C^*(h)$ given by

$$C^*(h) = \frac{Mes((X \cap Z) \ominus B)}{Mes(Z \ominus B)}.$$

(3.15)

The denominator, $Mes(Z \ominus B)$, is the total possible number of occurences of $B = \{0, h\}$ within the measuring window Z. The properties of $C(h)$ are: $C(0) = Pr\{x \in X\}$; $C(h) = C(-h)$; $C(0) \geq C(h)$.

3.6.3 Applications

The global covariance has been used to study the spatial distribution of cells in the embryonic ovary of a rat [10]. In this application, covariance was used to determine if the cells were uniformly distributed within the ovary. Once it was determined that they were clustered, the covariance was used at a smaller scale to measure the average distance between cell centers within each cluster.

The point covariance has been used to study the relation of wood structure to anisotropies of shrinkage during drying [36]. In this application, tree cross-sections were analyzed radially and tangentially, at several scales, to find correlations between the wood structure and its shrinkage patterns.

Chapter 4

Experiments with Real Range Imagery

This chapter begins with a discussion of the concept of a range image. Following this, the real range data is described and related MM algorithms are presented.

4.1   Range Images

The value associated with a point in a range image is proportional to the distance between the range sensor and the corresponding point in the 3-D physical world. A range image can be interpreted as a 2-D function having a 3-D graph which is actually an inverted version of the physical surface being imaged (Fig. 4.1). Thus, the operation of rolling a ball *above* the surface of the object corresponds to moving a hemispherical function *beneath* the image function (Fig. 4.1). This inversion of surfaces must be kept in mind when thinking intuitively about the notions of closing, opening, etc.
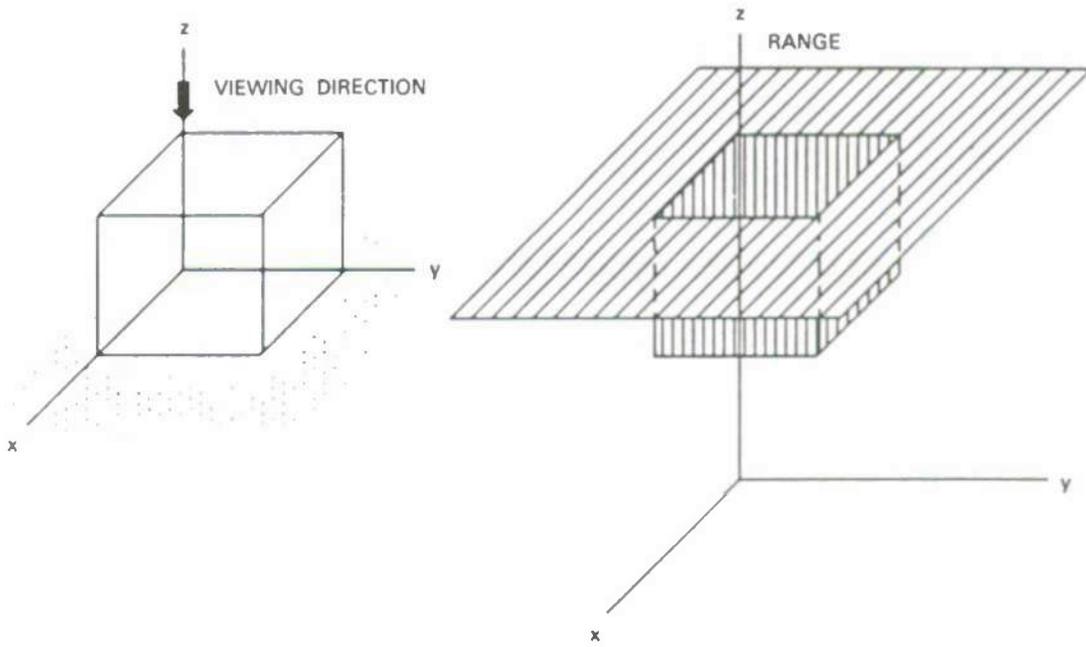
Figure 4.1. Range image generation.

33

4.2 Real Data

The real range images are obtained from a laser radar. For each pixel in a range image, a radar pulse is sent out into the world and the time between the transmission of the pulse and the reception of the reflected pulse is measured. If no reflection is received within a certain time window, the pixel is called a *dropout*. For other pixels, the value recorded is directly proportional to the distance to the reflection point in the world.

Since the data is quantized to 8 bits, each pixel value must be within the range 0-255. With this data set, the values 0, 1, 2, and 3 turn out to correspond to dropouts. Note that reflected pulses which are received too early are recorded as dropouts, as are reflections which are received too late (or not at all).

The radar used in this work scans a square section of the world, however, the output of the scanner is a rectangular image (128 × 60 pixels). This occurs because the vertical angular sampling interval of the scanner is twice that of the horizontal angular sampling interval. Because of this disparity, the original and processed images have been zoomed vertically by a factor of 2 for display purposes, although processing is performed on the original 128 × 60 pixel images. An example of an unzoomed real range image is shown on page 35.

4.3 Experiments

In this section, the problems of noise removal and 2-D feature extraction are addressed.

4.3.1 Noise Removal

There are two types of noise in the real range images: *dropouts* and *outliers*. As indicated above, dropouts have one of the values 0, 1, 2, or 3, thus, they appear as dark spots. Outlier pixels have values far from those of neighboring pixels and
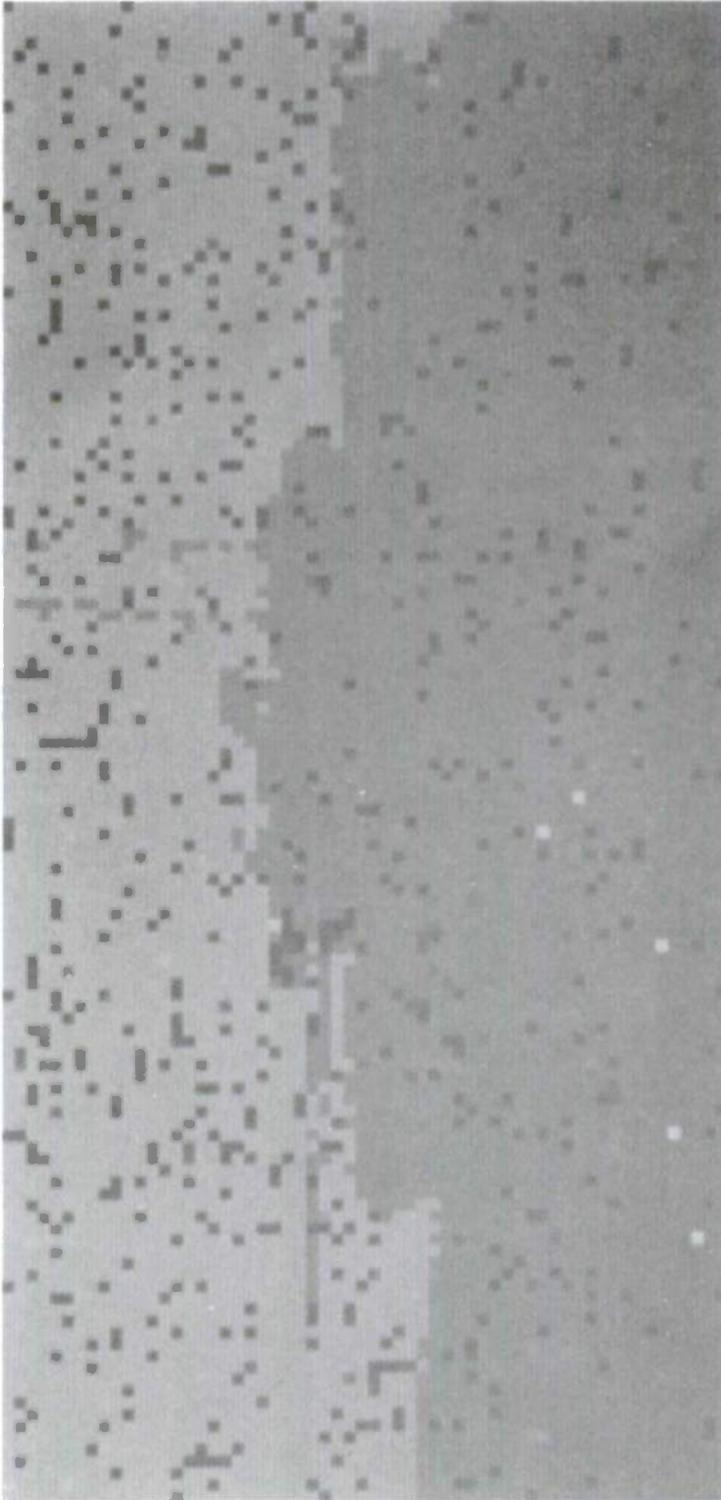
Typical real range image.

appear as both bright and dark spots. Since there are two different types of noise, two different methods of noise removal should be employed. In fact, the situation is even more complex since both dropouts and outliers can appear as dark spots. Therefore, blind removal of dark spots cannot be attempted before the dropouts are filled in. Thus, the proposed cleaning procedure is:

1. Remove outliers which appear as bright spots.

2. Fill in values for dropouts.

3. Remove outliers which appear as dark spots.

To perform these processing steps, only *function* MM and point operations are used. The results and the SEs which were used are shown on page 37. Each of the SEs is a flat 2-D function with value zero inside the region of support and origin marked O.

To remove the outliers which appear as bright spots, we take the pointwise minimum of the original, say i (p. 37-1), and its dilation $i \oplus \breve{a}$ (p. 37-2), i.e., $t = min(i, (i \oplus \breve{a}))$ (p. 37-3). If one looks at the formula for dilation (Eq. 2.15), the value of t at a point x, $t(x)$, can be expanded to

$$
\begin{aligned}
t(x) &= [min(i, (i \oplus \breve{a}))](x) = [min(i, (i \oplus a))](x) \\
&= min(i(x), max(i(x-y) + 0)) \qquad y \in Ros(a).
\end{aligned}
$$

By noting that $Ros(a)$ is a small donut-shaped SE, one sees that this operation has the effect of clipping the input i such that no pixel has a value greater than the maximum value of its four nearest neighbors.

To fill in the dropouts, we replace each of them by the corresponding value in the closing of t by b (p. 37-4), i.e.,

$$
u = \begin{cases} t^b & t \in \{0, 1, 2, 3\} \\ t & \text{otherwise.} \end{cases}
\tag{4.1}
$$

This has the effect of "patching up" the holes created by the dropouts (p. 37-5). Note that the region of support of b will determine the size of the patch. In this case the

36

STRUCTURING ELEMENTS

PROCEDURE

1. REMOVE OUTLIERS WHICH APPEAR AS BRIGHT SPOTS
2. FILL IN VALUES FOR DROPOUTS
3. REMOVE OUTLIERS WHICH APPEAR AS DARK SPOTS

- IMAGERY
  - REAL RANGE DATA
  - COARSE RESOLUTION
- NOISE
  - DROPOUTS
  - OUTLIERS
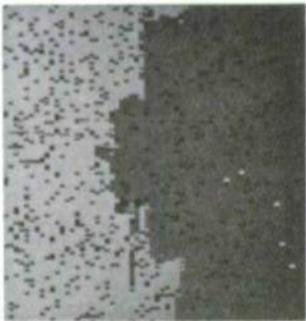
1: ORIGINAL
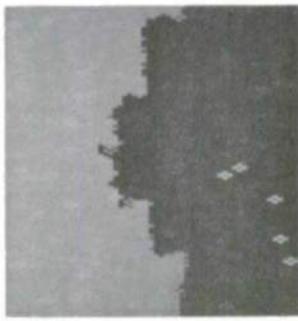
2: DILATION OF 1 BY a
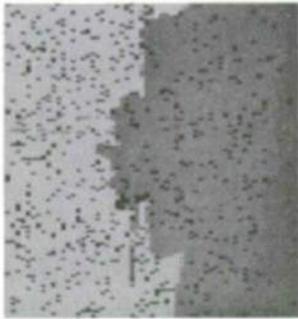
3: MINIMUM OF 1 AND 2
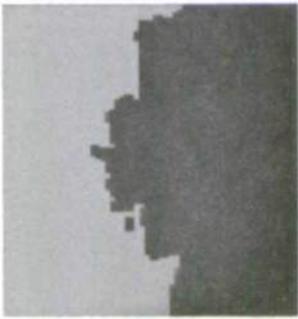
4: CLOSING OF 3 BY b
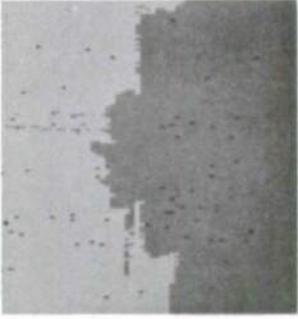
5: REPLACEMENT OF DROPOUTS
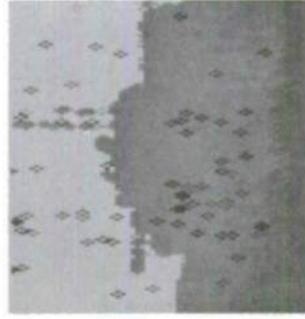
6: EROSION OF 5 BY a
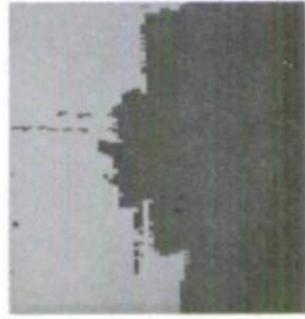
7: MAXIMUM OF 5 AND 6

Noise removal.

37

region of support of the SE is 4×2 pixels so any region of dropouts larger than this will not be patched. With our data, this SE was sufficient in almost all cases.

Lastly, the remaining outliers which appear as dark spots must be removed. This is accomplished in a manner completely analogous to that for removing bright spots. We take the pointwise maximum of u and its erosion $u \ominus \breve{a}$ (p. 37-6), i.e., $v = max(u, (u \ominus \breve{a}))$ (p. 37-7). If one looks at the formula for erosion (Eq. 2.16), the value of v at a point x, $v(x)$, can be expanded to

$$
\begin{aligned}
v(x) &= [max(u, (u \ominus \breve{a}))](x) = [max(u, (u \ominus a))](x) \\
&= max(u(x), min(u(x-y)+0)) \qquad y \in Ros(a).
\end{aligned}
$$

By noting that $Ros(a)$ is a small donut-shaped SE, one sees that this operation has the effect of clipping the input u such that no pixel has a value less than the minimum value of its four nearest neighbors.

About the SEs

One may wonder how the SEs for this application were chosen. For SE a, the region of support was chosen to cover the four nearest neighbors. The constant value of the function a was chosen to be zero; changing the constant value would have had the following effect. If the value corresponding to a was 6, the values of the function $i \oplus \breve{a}$ would have increased by 6; the values of the function $i \ominus \breve{a}$ would have decreased by 6. Thus, rather than clipping the outliers to within the max and min of the four nearest neighbors, they would have been clipped to within $max + 6$ and $min - 6$ of the four nearest neighbors.

The shape of SE b was chosen to "patch" up a region of the image of the same size or smaller. Though the value of the the function b was zero, it could have had any other constant value and the results would have been the same.

4.3.2 Feature Extraction

In most of the real range images, good features to use for recognition are characteristic object appendages such as antennas and guns. Their extraction is carried out on binary image silhouettes since the real range data provides only coarse 3-D information. A binary silhouette is produced by thresholding the gray-scale image (p. 40-1) at the median intensity value (p. 40-2). The proposed procedure for isolating the characteristic appendages of the silhouette is:

1. Isolate all appendages with widths similar to those of the characteristic appendages.

2. Join isolated appendages if they are within a given distance of each other.

3. Filter out any appendage which is too small to possibly be a characteristic appendage.

To perform these steps, only *set* MM and point operations are used. The results and the SEs used are shown on page 40.

To isolate all appendages we take the set difference of the original binary image, say I (p. 40-2), and its opening I_A (p. 40-3), i.e., $T = I - I_A = I \cap (I_A)^c$ (p. 40-4). Note that we have chosen A to be slightly larger than the appendages we wish to extract.

For joining isolated appendages, we use the closing $U = T^B$ (p. 40-5). All isolated appendages separated by gaps less than the size of B (4×2 pixels) will be joined together.

The last step is to filter out any appendages which are too small to merit further study. This filtering procedure is a two-step process. First, an image containing only those appendages (artifacts) which are to be filtered out is created. This is accomplished by using the hit-or-miss transformation and Minkowski addition. The hit-or-miss transformation will produce an image which is "true" (white) at every

39
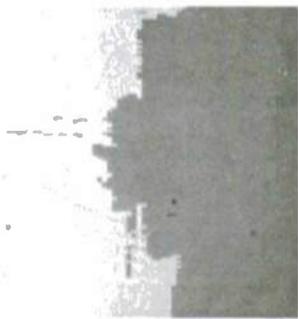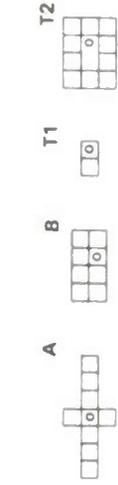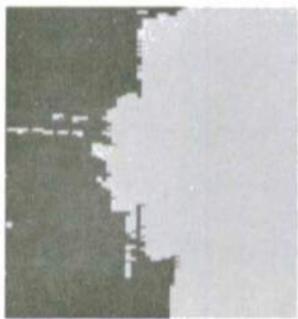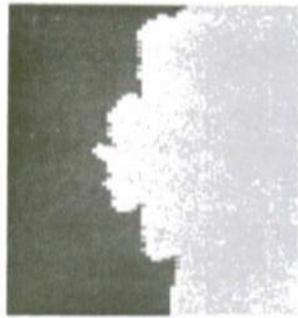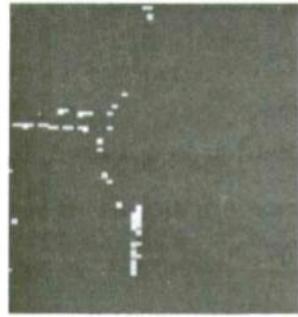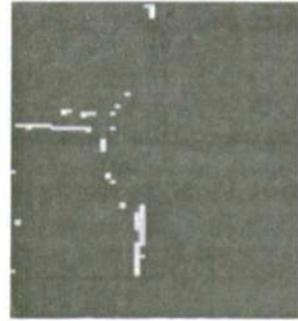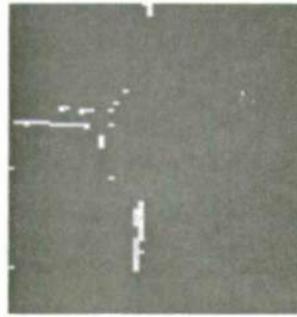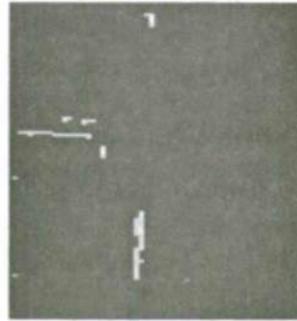
2-D feature extraction.

location where a given pattern $T1$ is located, provided $T2$ is chosen as the complement of $T1$ in a selected surrounding window [7] (p. 40-6). From this result, an image of removable artifacts can be created by replicating the pattern $T1$ at each "true" value in the hit-or-miss transformation, i.e., $V = (U \circledast (T1, T2)) \oplus T1$ (p. 40-7). The desired result is the set difference of the image of joined appendages U and the removable artifacts V, i.e., $W = U - V = U \cap V^c$ (p. 40-8). For our purposes, appendages which are as small as or smaller than 2×1 are filtered out. This implies two filterings; one for 2×1 pixel appendages and another for 1×1 pixel appendages. The intermediate steps for filtering out the 2×1 pixel appendages are shown in p. 40-6 through p. 40-8. The final result, after filtering out the 1×1 appendages, is shown in (p. 40-9). It should also be noted that if the approximate object orientation is known, MM techniques could also be used to distinguish between vertical and horizontal appendages. This is discussed further in the next subsection of this chapter.

About the SEs

SE A was chosen large enough so that it would not fit in the appendage region, yet small enough that it would fit in the body region. SE B was chosen so that it would connect pixels within 4 pixels horizontally, 2 pixels vertically. Ideally, A, B, and $(T1, T2)$ should be symmetric. In terms of the geometry of the world, they *are* symmetric but *appear* non-symmetric because the horizontal angular sampling interval is one half that of the vertical angular sampling interval.

4.3.3 More Examples

With the previous feature extraction method, no knowledge of object orientation was assumed. However, under certain circumstances, some assumption may be made about object orientation, e.g. one can assume that an object lies on a nearly horizontal surface. In that case, one may be able to reconnect and/or extract appendages at characteristic orientations. MM algorithms which incorporate *a priori* orientation

information are presented in the following paragraphs and typical results are shown on pages 43-44 and pages 46-47.

The first example, on pages 43-44, shows techniques of *function* MM and point operations applied to a real range image. The goal is to extract the object of interest from the original image and to reconnect broken appendages. The SEs (or kernels) which are used are labelled 1 through 7. SEs 1 and 3 are small ellipsoids; the other SEs are rectangles of various sizes. Results at each stage in the processing are shown in photos A-K along with a description of the operations performed. The following is a high-level description of the algorithm.

First, a relatively clean range image[1] , A, is closed by a small half-sphere slightly larger that the widths of the gun and antennas. This removes the appendages (B). Note that there is one location along the gun barrel where the SE "fell into the gun valley" thereby leaving a mark (the "cross") directly related to the shape of the SE. Next, the vehicle body remaining in image B is "shaved off" (C) by using a very long SE which must be longer than the body length.

After pointwise subtraction of C from B, all that is left (D) is the object plus some ground clutter, which is subsequently removed (E) by closing by a small vertical SE with length slightly larger than that of the largest clutter height. Image E therefore contains the isolated body. Similarly, pointwise subtraction of B from A produces a noisy image F of the isolated broken appendages (gun and antennas).

This image is now processed with two independent sequences of opening followed by closing. In the first, opening with the small vertical SE reconnects the antenna fragments by eliminating the peaks between them, while subsequent closing with a slightly longer SE eliminates vertical appendages which are too short. The end result (H) is a pair of less fragmented antennas, no gun, and very little noise. The other sequence is very similar, but uses horizontal SE's: the result in J shows the gun, no antennas, and very little noise. By pointwise addition of the body image E, the

---

[1] The cleaning procedure is described in [69].

Application of function MM.
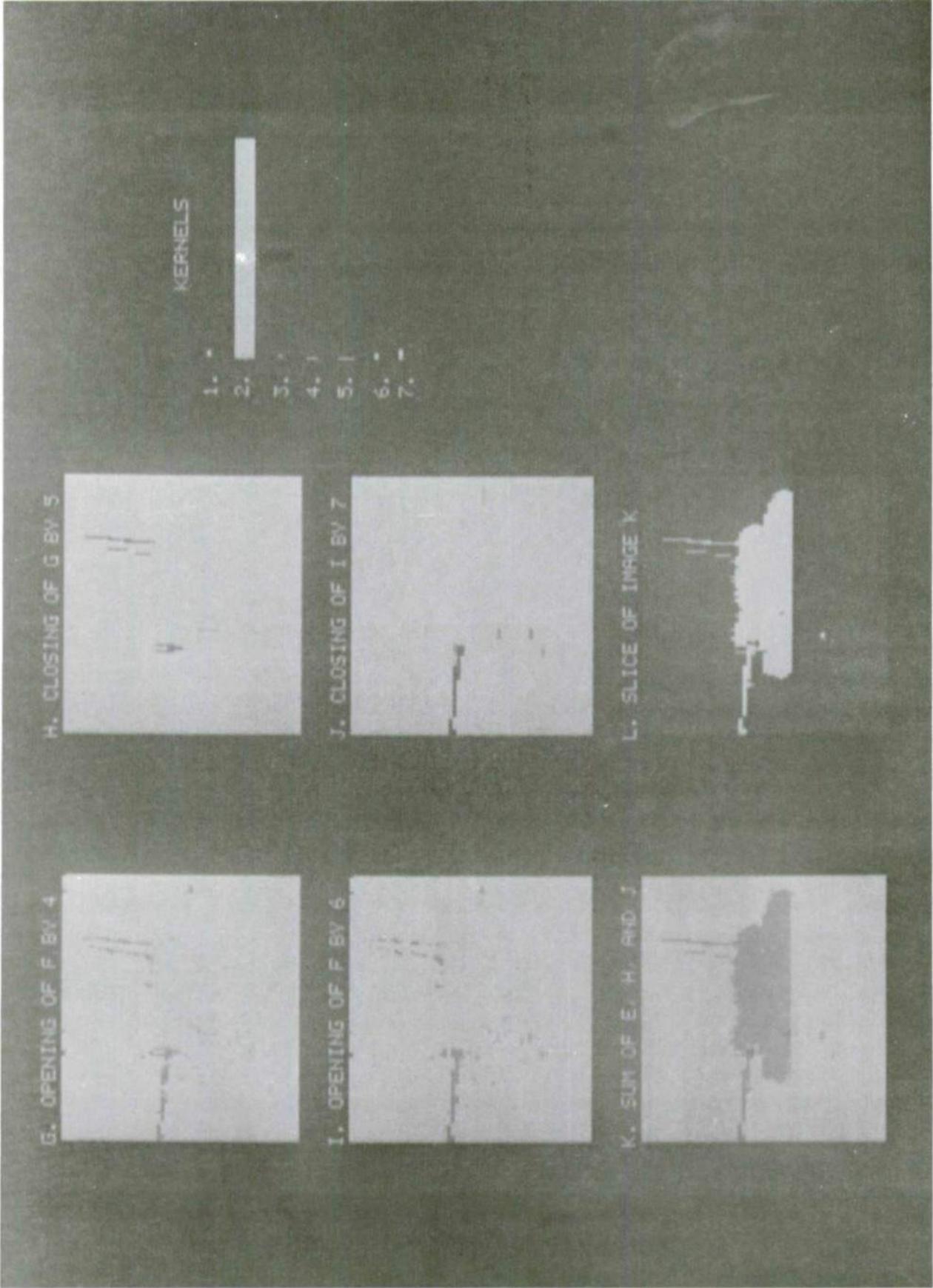
Application of function MM (continued).

44

antenna image H, and the gun image J, one obtains the reconstituted object with less fragmented appendages (K). Image L is simply a histogram-based segmentation of K into two regions.

For completeness, it should be noted that a very similar processing sequence has been inserted in the processing chain described in [69] to reconnect appendages prior to edge detection. This additional processing generally results in better range silhouette extraction.

One can also use a similar algorithm using *set* MM to extract the object and reconnect broken appendages. The results of this processing are shown on pages 46-47. The SEs which are used are labelled 1 through 8. SEs 1 and 4 are small ellipses; the other SEs are rectangles of various sizes. Results at each stage in the processing are shown in photos A-N along with a description of the operations performed. The following is a brief description of the algorithm.

The first step is to create a binary image from the original (A) through a segmentation procedure. This procedure gives a silhouette of the object with many holes and ground clutter (B). The holes are filled by closing by a small disk (C). The appendages are removed by the opening, giving an image of the object body (D). The next step is to detect a continuous horizontal band larger than the body, which corresponds to ground clutter. To accomplish this, the image of the body (D) is opened by a long, horizontal SE. Once the band (E) is located, it is dilated by a long vertical SE so that the lower half of the image (where the ground clutter appears) is entirely filled (F). This image of ground clutter can be subtracted from the image of the body and ground clutter (D) to give an image of the body and some residual ground clutter (G). From this step on, the extraction and reconnection of the gun and antenna is entirely analogous to the procedure outlined for the gray-scale case and the end result (N) is very similar.

Application of set MM.

46

H. OPENING OF G BY 4   I. C AND (NOT (D OR F))

J. CLOSING OF I BY 5   K. OPENING OF J BY 6

L. CLOSING OF I BY 7   M. OPENING OF L BY 8

N. H OR K OR M

KERNELS

1. +
2.
3.
4. +
5.
6.
7.
8.
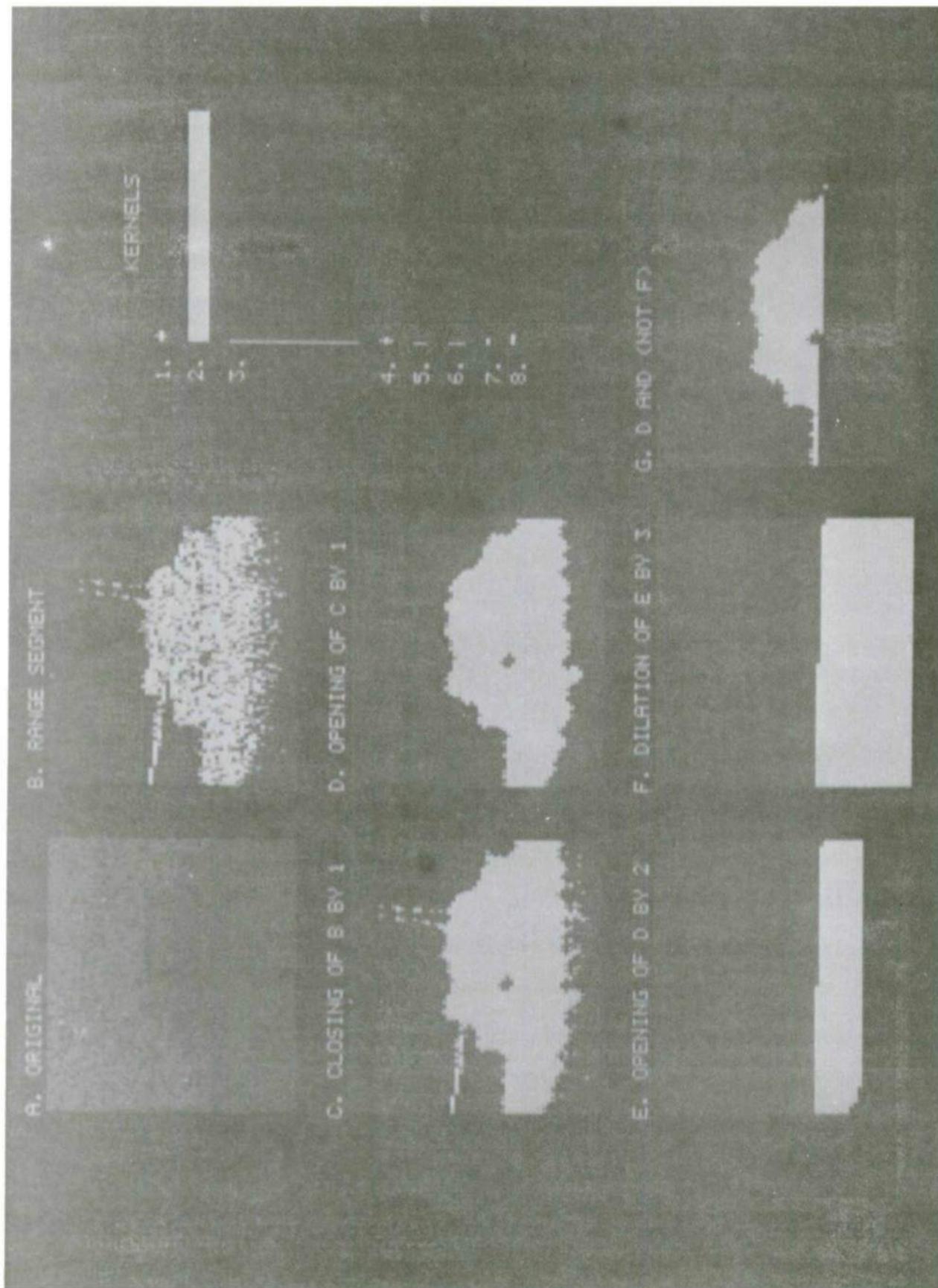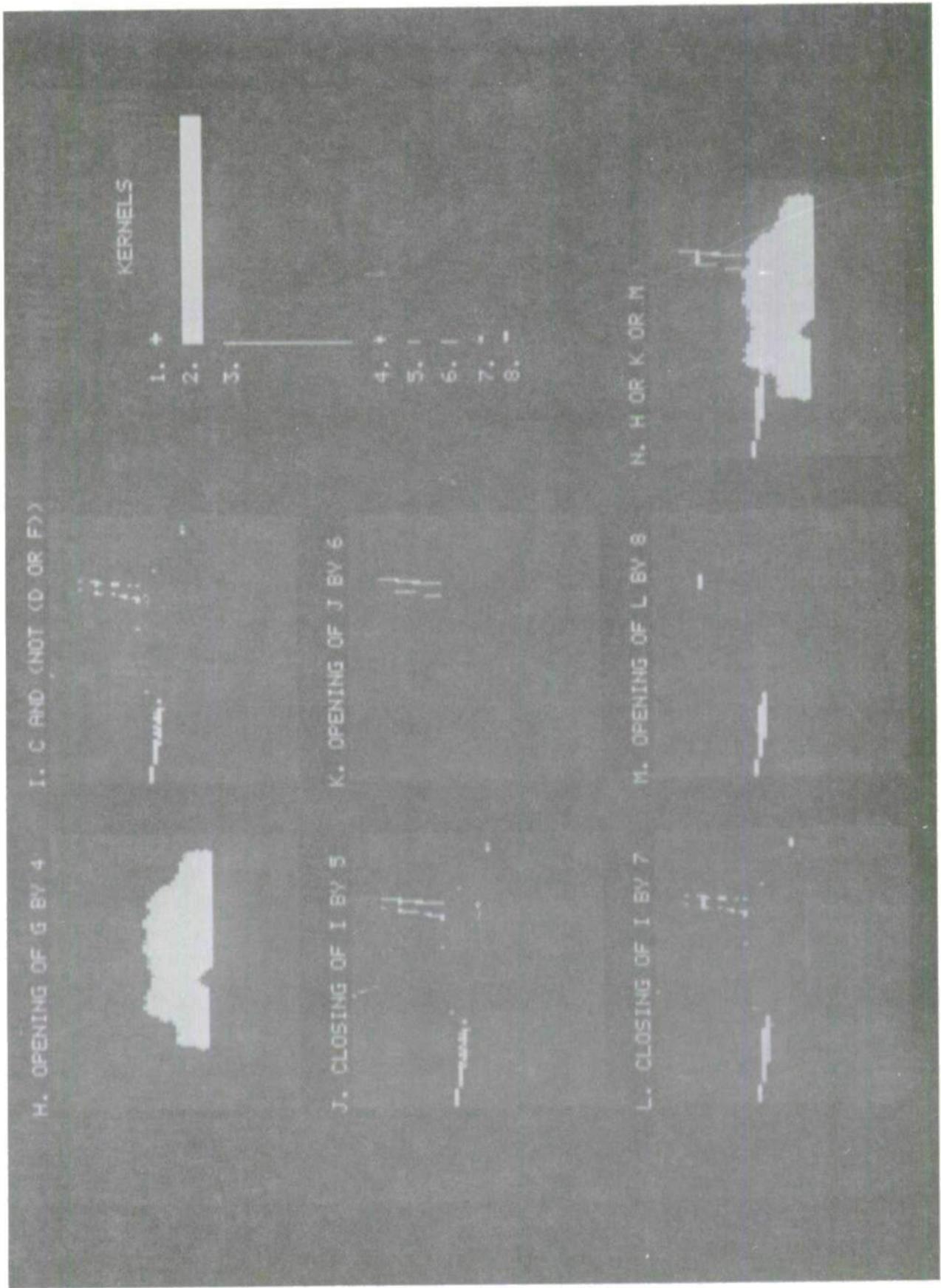
Application of set MM (continued).

47

Chapter 5

Experiments with Synthetic Range Imagery

Although MM techniques give fairly good feature extraction results with the real data, they are limited by several factors. The coarse range resolution of the real data does not provide much information on the 3-D structure of the objects of interest; it provides only rough silhouettes. Thus, an object cannot be easily identified if its characteristic appendages do not appear on the silhouette. Also, the angular resolution is very coarse compared to the dimensions of the objects of interest. This makes it difficult to distinguish between guns and antennas since they have approximately the same diameter (1 or 2 pixels). It is thus natural to ask how MM feature extraction techniques would work on data with higher resolution in range and angular dimensions. To have complete flexibility in investigating this question, a synthetic range image generator was developed.

5.1 Data

The synthetic range images are produced from a description of the surface of an object in terms of triangular facets, thus all objects in the images are polyhedra. The

polyhedral objects under study are free floating in space in front of a background plane perpendicular to the viewing direction. The horizontal and vertical angular sampling intervals are both one half the horizontal angular sampling interval of the real data, therefore zooming is not needed for display. The range resolution of the synthetic data is 60 times better than that of the real data, and the distance to the object is approximately the same as that for the real data.

5.2 Experiments

In the next two subsections, the synthetic data is used to explore the problems of 3-D feature extraction and corner extraction.

5.2.1 Feature Extraction

An example of a synthetic range image is shown in (p. 50-1). Note that none of the characteristic appendages (gun, antenna) appear on the silhouette, and that they have distinguishable differences in thickness.

We can use techniques from *function* MM to extract characteristic appendages from the synthetic data . The proposed procedure is:

1. Find guns.

2. Find antennas.

The results and the SEs used are shown on page 50. Each SE is a 2-D function whose 3-D graph is a half-sphere.

To find the gun, we subtract the original image, say i (p. 50-1), from the closing i^a, i.e., $t = i^a - i = RB^a(i)$ (p. 50-2). Conceptually, this has the same effect as rolling a ball around on the upper surface of the 3-D graph corresponding to the range image and retaining the places where the ball does not fit. If the ball is slightly bigger than the diameter of the gun, the gun will show up in the result. The next step is to remove

STRUCTURING ELEMENTS
HEMISPHERES
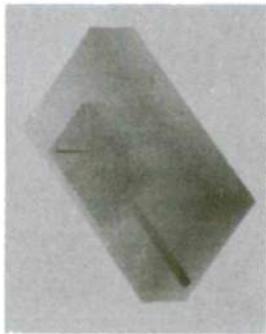
PROCEDURE

- IMAGERY
  - SYNTHETIC RANGE DATA
  - POLYHEDRAL OBJECTS
  - HIGH RESOLUTION
- 3-D FEATURES
  - OBJECT APPENDAGES

1. FIND THICK APPENDAGES
2. FIND THIN APPENDAGES

1: ORIGINAL
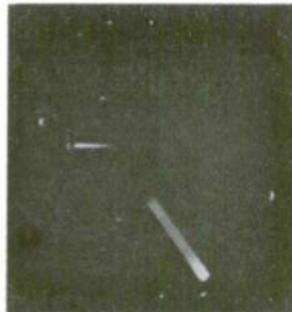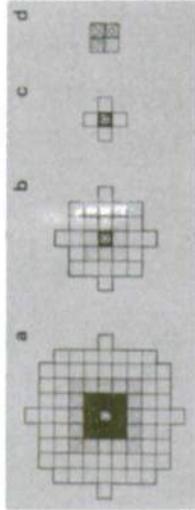
2: CLOSING OF 1 BY a, MINUS 1

3: OPENING OF 2 BY b

4: CLOSING OF 1 BY c, MINUS 1
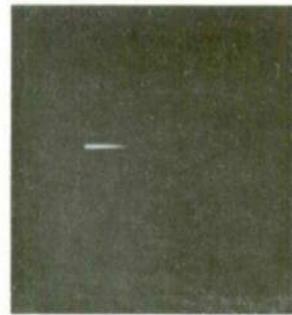
5: OPENING OF 4 BY d

3-D feature extraction.

appendages and artifacts which have a diameter slightly less than that of the gun. This is accomplished by the opening $u = t_b$ (p. 50-3).

We can locate the antenna in the same way. This time we use SE c which has a diameter slightly larger than the antenna, so $v = i^c - i = RB^c(i)$ (p. 50-4). Again, we can remove any artifacts with diameter smaller than that of the antenna by the opening $w = v_d$ (p. 50-5).

About the SEs

The choice of SEs for feature extraction was relatively easy. Hemispherical functions were chosen so that processing would be independent of orientation. The sizes of a and b were chosen according to the thickness of the gun and together they form a "size-pass filter," passing only appendages smaller than a but larger than b. The SEs c and d were selected as components of a smaller "size-pass filter", according to the thickness of the antenna.

5.2.2   Corner Extraction

With the previous methods of feature extraction, it is assumed that an object has some distinguishable appendage. If this is not the case, another feature which can assist the recognition of man-made objects is the 3-D corner. Corner detection algorithms can be readily tested on images produced by the synthetic data generator. This subsection describes an algorithm developed to locate convex[1] polyhedral corners (vertices) in high-resolution range images. The results of the corner extraction and the SEs used are shown on pages 52 and 53. SE a is a hemispherical function; B and C are 2-D sets. The other SEs are thinning SEs.

The object selected for this experiment is a cube and the corresponding range

---

[1]Convex corners were chosen for discussion purposes; a minor change to the algorithm would provide for extraction of concave corners. The case where both convex and concave corners are present in the same image is not addressed here.

DETECTION

STRUCTURING ELEMENTS

a (Sphere)   b   c (Disk)

THINNING   PRUNING   DETECTION

- IMAGERY
  - SYNTHETIC RANGE DATA
  - PDLYHEDRAL DBJECTS (Convex)
- CORNERS
  - HIDDEN-FACET (Double-Joins And Triple-Joins)
  - EXPOSED-FACET (Triple-Joins)

PROCEDURE

1. DETECT HIDDEN-FACET CORNERS
2. DETECT MDST TRIPLE-JOIN CORNERS
3. COMBINE RESULTS

1. ORIGINAL

2. TWO TYPES OF CORNERS
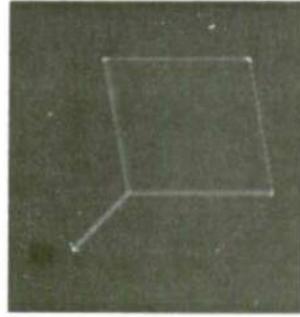
3. CLOSING OF 1 BY a, MINUS 1 (Rolling-Ball)

4. AFTER THRESHOLDING 3, DILATION BY b (H-Corners)

5. AFTER THRESHOLDING 3 AT 0, DILATION BY b

6. THINNING AND PRUNING OF 5 VIA HIT-OR-MISS

7. DETECTION OF TRIPLE-JOINS VIA HIT-OR-MISS

8. DILATION OF 7 BY c (Most Triple-Join Corners)

9. LOGICAL OR OF 4 AND 8

3-D corner extraction.

52

ORIGINALS

DETECTED CORNERS

LOCALIZED CORNERS AND EXPOSED-FACET CORNER MEASUREMENT

3- D corner extraction(continued).

53
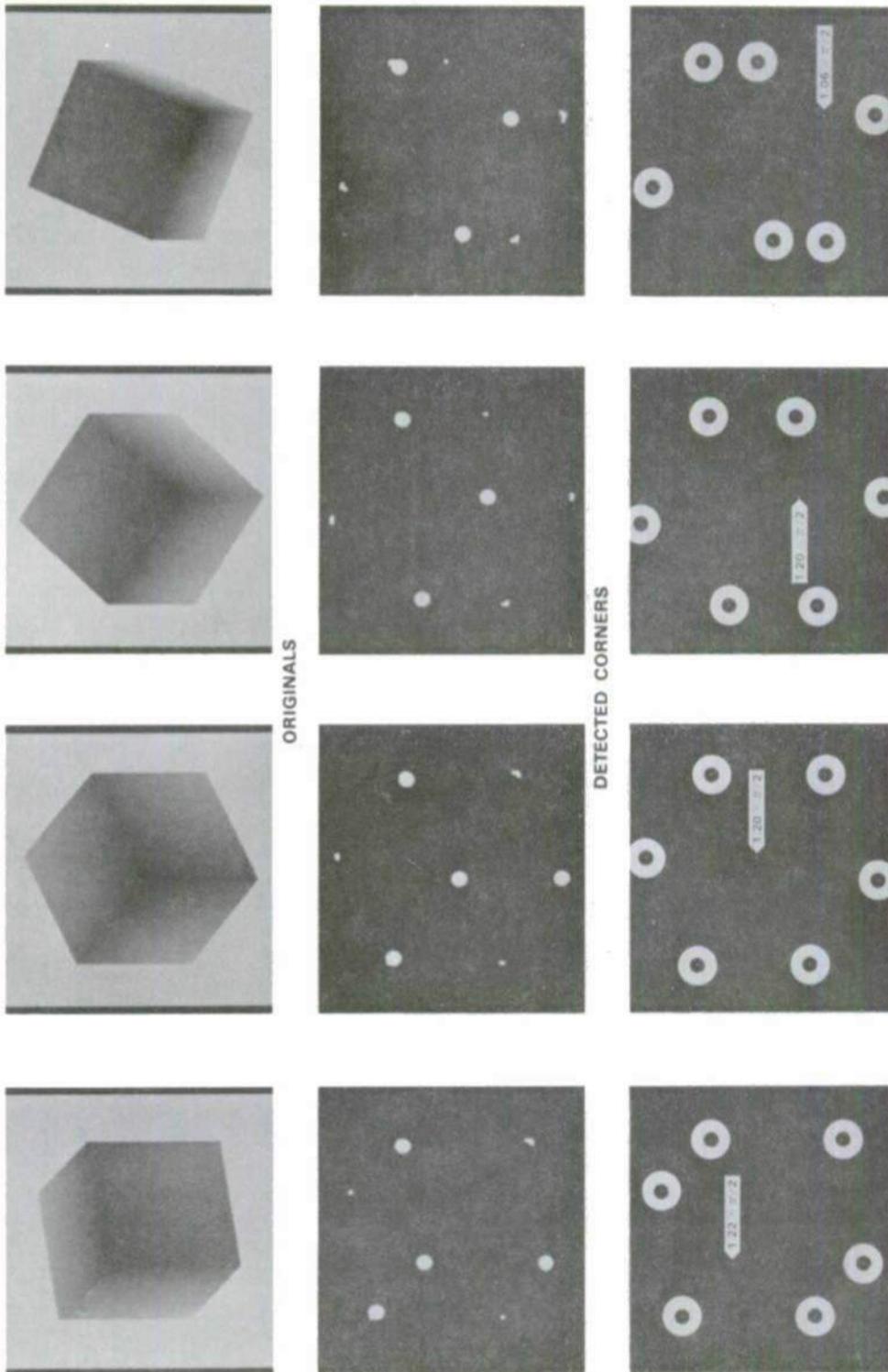
image is shown in p. 52-1. The corners of any polyhedral object at a given orientation can be divided into two categories: exposed-facet corners (E-corners) and hidden-facet corners (H-corners). This is illustrated in p. 52-2 for the selected view of the cube. It should be noted that the labelling of corners varies as the viewing direction is changed. With this in mind, the problem solving approach is as follows:

1. Detect corner regions.

2. Localize corners.

The first step is to find the approximate location of corners of each type. The first type of corner to be detected is the H-corner. These corners appear on the occluding boundary of the object and can be detected using the rolling ball transform. The SE used in the rolling ball transform is the hemispherical function a. If the input image is denoted i (p. 52-1), the result of the rolling ball transform is $t = RB^a(i)$ (p. 52-3). If the object of interest stands out from its background (such as an airplane against the sky), the rolling ball will produce large peaks near corners on the occluding boundary. To understand this, refer to Figure 5.1 which shows the top view of a cube in the vicinity of an H-corner. To compute the rolling ball transform, one can either consider a ball rolling on the top surface of the corresponding range image (and a closing), or a ball rolling on the bottom of the combined object/background surface (and an opening). The second approach is taken in Figure 5.1, where the lengths of the parallel segments shown on the graphs at the bottom correspond to the values of the transform along two of its cross-sections. Clearly, the maximum values are found near the corner and constitute a ridge of constant values. Assuming that this ridge is higher than peaks produced by vertical (toward the viewer) object protrusions, the H-corners are easily found by thresholding t, producing a binary image with "ones" at points where $t >$ threshold. This binary image is then dilated by SE B to produce an image of detected H-corner regions (p. 52-4). The dilation by B accounts for effects of discretization which can cause fragmentation of the corner regions. This effect is discussed in the paragraph below titled, **"About the SEs."**

54

TOP VIEW

PEAKS

PEAKS

TOP

CUBE

BACKGROUND

PEAKS

CROSS-SECTION bb'

TOP

CUBE

BACKGROUND

PEAK

CROSS-SECTION aa'
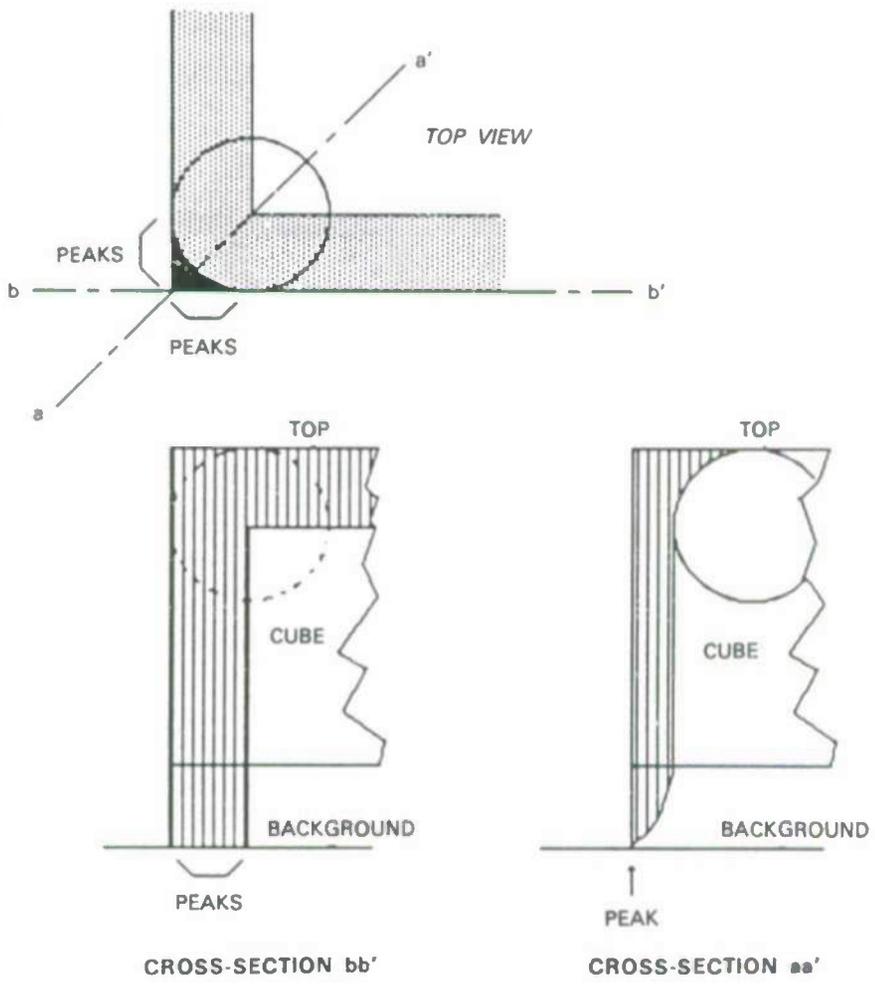
Figure 5.1.   Peaks in the rolling ball transform.
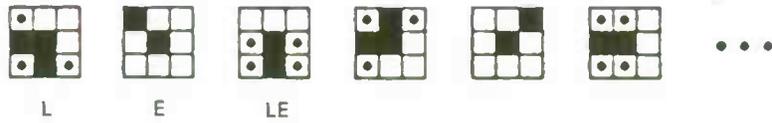
Figure 5.2. $\left\{L, E, LE\right\}\infty$.
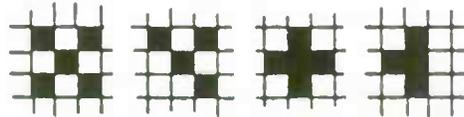
Figure 5.3. Pixel patterns indicating the presence of corners.

The next step is to detect E-corners. If one had a line drawing of a polyhedron (with hidden lines removed), one would notice that all exposed-facet corners (E-corners) appear in the drawing at the intersection of three or more edges (p. 52-2). Thus, with a line drawing of a polyhedron, one can detect E-corners (and some H-corners) by detecting these edge intersections. This is the approach taken to detect E-corners.

The line drawing is obtained in the following way: first, the rolling ball transform of the input i, $RB^a(i)$, is thresholded at zero. The "ones" in this binary image indicate pixels where $RB^a(i) > 0$. This binary image T is then dilated by B to correct for any artifacts caused by digitization, giving $U = T \oplus \check{B}$ (p. 52-5). U is then thinned by the infinite sequence of 90-degree rotations of the hit-or-miss SEs L, E, and LE[2] (Fig. 5.2), denoted $\{L, E, LE\}_\infty$. This produces the thin line drawing $V = U \bigcirc \{L, E, LE\}_\infty$ (p. 52-6).

The hit-or-miss transformation can be used to detect the pixel patterns in the thinning, V, which indicate the presence of edge intersections. Examples of these patterns are shown in Figure 5.3. Each of these patterns has one thing in common—the pixel neighborhood, when read in a clockwise or counterclockwise direction, *contains* the

---

[2]This notation is motivated by the Golay alphabet [62], though it is not identical.
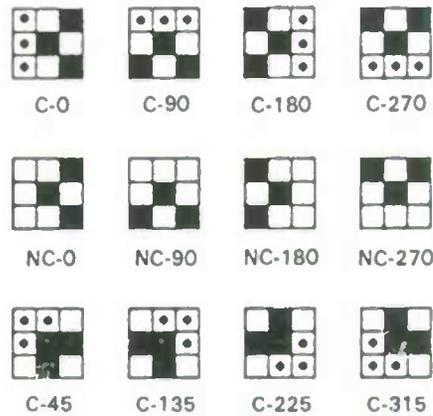
Figure 5.4.   Corner-detecting SEs.

sequence 0,1,0,1,0 (black = 1). In most cases, this pattern indicates the intersection of three or more edges, however there is one pixel configuration[3] which matches this pattern yet does not correspond to the intersection of three or more edges (Fig. 5.4, NC-0). Thus, the hit-or-miss transformation with the four 90-degree rotations of C-0 (Fig. 5.4), denoted {C-0, C-90, C-180, C-270}, gives edge-intersection locations and also some "false alarms" (occurences of the four rotations of NC-0). To eliminate these "false alarms," one can subtract out occurences of the four 90-degree rotations of NC-0, denoted {NC-0, NC-90, NC-180, NC-270}. The rest of the edge intersections are found using the hit-or-miss transformation with the four 90-degree rotations of C-45 (Fig. 5.4), denoted {C-45, C-135, C-225, C-315}. Thus, the edge intersections, W, are extracted from the thinning, V, according to the following:

$$W = ((V \circledast \{\text{C-0}, \ldots \text{C-270}\})/(V \circledast \{\text{NC-0}, \ldots \text{NC-270}\})) \cup (V \circledast \{\text{C-45}, \ldots \text{C-315}\})$$

$$(5.1)$$

The binary image W (p. 52-7)[4] is "true" near the intersections of three or more

---

[3]One can find *other* neighborhoods which obey this condition and are *not* edge intersections. Under more careful observation, however, one will find that these configurations are not possible after thinning with $\{L, E, LE\}_\infty$ is performed.

[4]The large, thick "donuts" in p. 52-7 are intended only to draw attention to the single-pixel E-corner locations. They are not part of the image.

57
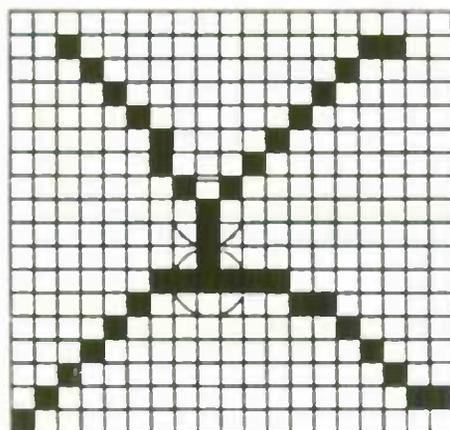
Figure 5.5.   Several responses for one corner.

edges, yet the locations of these "true" points generally does not coincide with the exact locations of corners[5].   Also, the intersection of more than three edges at a corner will, in general, produce several "true" values corresponding to the same corner (Fig. 5.5). To solve these problems, the image W can be dilated by a disk C. This transforms the image W from *points* to *regions* corresponding to the presence of corners (p. 52-8).

It is now a simple matter to combine the image of the H-corner regions (p. 52-4) and the image of edge-intersection regions[6] (p. 52-8) to get an image of all corner regions (p. 52-9).

After the corner regions are labelled[7], localization is accomplished by selecting the point within each region where the curvature is greatest. The curvature is measured as follows (see Figure 5.6 for an example in 1-D):

1. A point of the corner region is selected.

---

[5]This is due to asymmetries in the thinning process.

[6]Note: The E-corner regions constitute a subset of the edge-intersection regions.

[7]Although the MM algorithm for region labelling (Section 3.2) could have been used, running it on a sequential, general purpose computer is very slow. Thus, a simple labeller described by Winston and Horn ([70] p. 131) is used for this step.

58
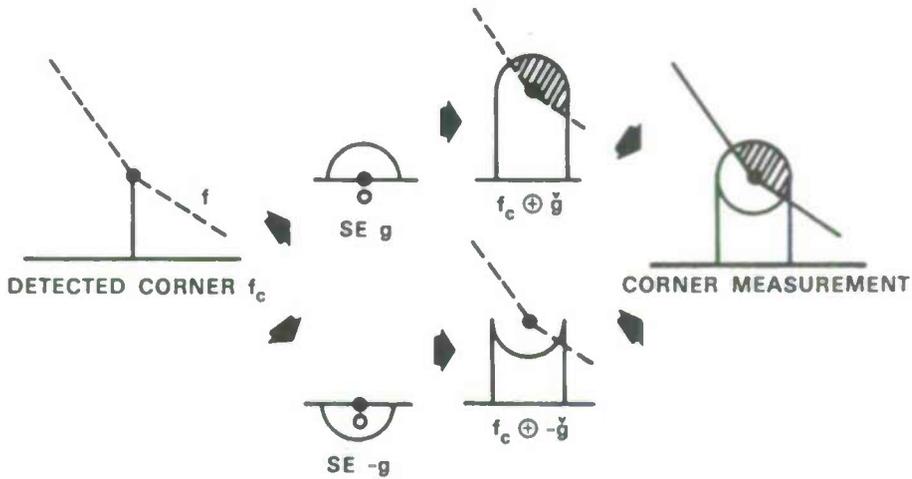
Figure 5.6. Corner measurement.

2. The corresponding point f_c in the range image f is dilated by a hemisphere g and also by an inverted hemisphere $-g$.

3. The curvature is computed according to the following formula:

$$\frac{\sum_{((f_c \oplus \check{g})-f)>0}((f_c \oplus \check{g}) - f) - \sum_{((f_c \oplus -\check{g})-f)>0}((f_c \oplus -\check{g}) - f)}{2 \times \sum g} \times 4\pi. \qquad (5.2)$$

This gives an estimate of the number of steradians taken up by the surface f at each point in the corner region. The point which takes up the minimum number of steradians is the located corner.

Results

The results of the corner extraction are shown on page 53. The originals are all different rotations of the same cube. The detected corner regions show up on the second row of photographs, and the localized corners show up on the last row. The E-corners are labelled by the number of steradians that they take up, as measured from the original range images. Ideally, the measurement should be precisely equal

59
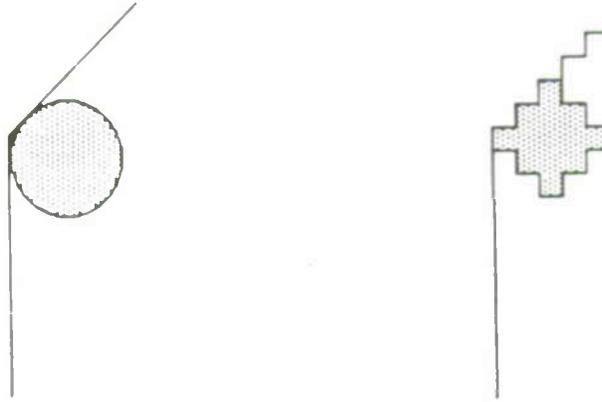
Figure 5.7.   Digitization effects.

to $\pi/2$ independent of orientation. It should be noted that this ideal result may be hard to obtain when distortions due to perspective are important.

About the SEs

The hemispherical SE a was selected for the rolling ball transform, $RB^a(i)$, for several reasons:

- It is rotationally symmetric.

- Its radius of seven pixels is large enough to *not* fit in most polyhedral edges.

If the radius is too small, the rolling ball transform will not pick up edges. This is due to digitization effects which allow a digital ball to "fit" in regions beneath a digital surface where a continuous ball would not fit beneath the corresponding continuous surface (see Fig. 5.7).

The smoothing SE, B, was chosen to reduce fragmentation artifacts produced by digitization. An example of such artifacts appearing in the digital case, but not in the continuous case, is shown in Figure 5.8. It is clear that different choices for the SE a will create different fragmentation artifacts. Thus, the choice of B is directly related to that of a.

The SE C, used to dilate the edge-intersection locations, W, of the thinning, V, was selected because:

60

FRAGMENTED
CORNER REGION

Figure 5.8.   Digital artifacts.
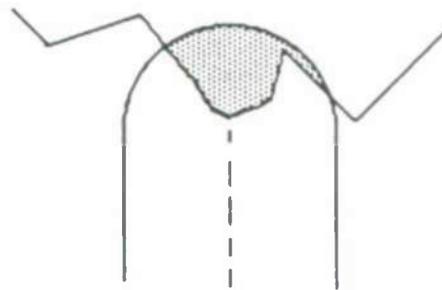
Figure 5.9.   Corners overlapped by the corner-measuring SE.

- It is rotationally symmetric.

- It is assumed that the edge-intersection locations in the thinning, V, are not more than the radius of a (seven pixels) away from the exact corner locations. This is the case in general.

The hemispherical corner-measuring SE, a, was selected because its radius was large enough to provide a good estimate of the curvature, yet small enough to avoid overlapping several corners at one time. An example of this problem is shown in Figure 5.9.

61
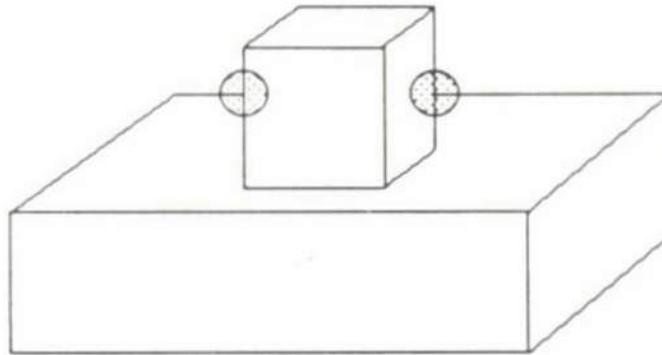
Figure 5.10.   Ambiguities from edge intersections.

Limitations

Besides the limitations which arise because of digitization problems, it should be pointed out that the corner extraction algorithm will clearly not work (in its present state) for a general polyhedron. If a polyhedron is not convex, edge intersections may not correspond to corners (Fig. 5.10). This would lead to erroneous results since the algorithm relies on the assumption that edge intersections correspond to either E-corners or H-corners. To solve this problem, one would have to select another approach.

Chapter 6

Conclusion

MM provides good techniques for geometric signal analysis. This is particularly important for range imagery where there is a direct correspondence between the data and the geometry of the world. Once an image feature has been specified geometrically, it can be extracted using MM. This has been demonstrated particularly well with the appendage and corner extraction algorithms of Chapters 5.

In Chapter 4, function MM proved useful for removing noise from real range images and, because of the limited resolution of the real data, both function and set MM techniques proved useful for feature extraction. It was also shown that the success of morphological techniques is directly related to the degree of *a priori* knowledge of the signal feature to be extracted. Without knowledge of the approximate orientation of an object, one is restricted to using rotationally symmetric SEs.

In Chapter 5, function MM proved useful for 3-D appendage and corner feature extraction from high resolution synthetic images. Even in this "ideal" case, however, digitization problems affected the performance of MM techniques. As was noted, the geometry of an object in the real world can be quite different from that in the corresponding digital range image. This problem is especially significant when a feature of interest corresponds to just a few pixels.

In spite of its limitations, MM has high potential for machine vision applications.

The basic operations of MM satisfy the criteria of being *general* and *parallel.* As we have seen in Chapters 3, 4, and 5, algorithms for texture analysis, image coding, noise removal, and feature extraction can all be described within the formalism of MM. This fact, along with solid theoretical foundations and nice implementation properties, make the basic operations of MM highly promising candidates for hardware implementation. At this point in time, architectures such as the Cytocomputer [50] and the CLIP [53] can support the basic MM operations. The MM algorithms for noise removal and 2-D feature extraction have also been implemented by the authors on a *wafer-scale*, parallel image processor simulator. For machines that can access only a local pixel window, the optimal decomposition of SEs becomes an important task in MM algorithm development. Zhuang and Haralick [46] have recently solved this problem for set MM SEs, however, the decomposition of function MM SEs remains an open research problem.

In conclusion, the operations of MM satisfy the criteria set forth for desirable machine vision operators: they are general and can be implemented in parallel. They are designed for geometric signal analysis and herein lies both the strength and weakness of MM-based approaches to vision. Although the techniques of MM *alone* will not enable a computer to see, they go a long way toward this goal.

Bibliography

This listing of papers consists of four sections: MM algorithms, MM architectures, work related to MM, and miscellaneous references. If there is no summary after a listing, it simply means that the paper has not been reviewed.

Algorithms

[1] Ankeny, L.A., *The Design and Performance Characteristics of a Cellular Logic 3-D Image Classification Processor*, Ph. D. Thesis, AF Inst. of Tech., April, 1981.

A processor architecture is developed to classify objects from synthetic range data. Range images of 3 objects on a flat surface are thresholded to produce binary images representing slices of 3-D space. The shapes resulting from the thresholding are circles and rectangles which are used for classification through a sequence of MM transformations. The circle measurements are produced from erosions with different circular SEs. The size and shape of the rectangles is measured through an erosion sequence, the medial axis transformation, and end erosion. For both circle and rectangle measurements, Ankeny introduces the notion of a residue set spread. This is a gauge of how well a SE fits inside digitizations of a continous object.

[2] Briot, M.; Robert de Saint Vincent, A., "La Vision des Robots," Vol. **16**, *La Recherche*, No. 170, pp. 1264-72, Oct., 1985 (in French).

The goal of this application is to identify RS-232 type connectors and associated cables in a scene. First, the connectors alone are extracted by segmentation based on intensity and region selection using global characteristics such as area and perimeter. Then, the cables which generally appear as dark, narrow, and arbitrarily curved regions are extracted from the original image using MM. Finally, skeletons are computed using MM and any region whose skeleton does not intersect one of the previously extracted connectors is discarded. The union of the extracted connector and cable regions is the final result.

[3] Chermant, J.L.; Coster, M.; Jernot, J.P.; Dupain, J.L., "Morphological Analysis of Sintering," *J. Microsc.* (GB), Vol. **121**, Pt. 1, pp. 89-98, Jan., 1981.

MM is used to describe the microstructural changes of metal powders during sintering (heating without melting). The analysis involves the observation of the connectivity number to distinguish the various stages of sintering. Also, the growth of "necks" between particles is tracked using MM.

[4] Chermant, J.L.; Coster, M.; Jernot, J.P., "Application of Quantitative Metallography to Sintering Investigations: Contribution of Image Analysis to Solid State Sintering Investigations," *Prakt. Met.*, Vol. **21**, No. 11, pp. 567-80, Nov., 1984.

MM is used to study changes in metal powders during sintering. These changes, which include bonding between particles, neck growth, and rounding of pores, can be used to distinguish the various phases of sintering. This analysis involves the use of MM to compute such quantities as the connectivity number and the size distribution of particles. No specific algorithms are described.

[5] Chernyavskii, K. S., "Mathematical Morphology – New Method for Analyzing Structures of Metals and Alloys (Review)," *Zavod. Lab.* (USSR), English trans. in *Ind. Lab.* (USA), Vol. **48**, No. 10, pp. 966-76, Oct., 1982.

This paper is an overview of MM techniques used in metallurgy.

[6] Coleman, E.N.; Sampson, R.E., "Acquisition of Randomly Oriented Workpieces Through Structure Mating," *IEEE Proc. CVPR*, San Francisco, Ca., pp. 350-357, 1985.

Range images of workpieces in a bin are analyzed to find stable gripping points. The algorithm involves:

- Noise removal. This involves a donut-shaped SE for noise spike removal and median filtering.
- Identification of pallet dividers and slots. This involves using long, narrow SEs for detection of pallet dividers. The slots (the area between dividers) are found using the medial axis transform.
- Identification of full slots. Full slots are identified by averaging the range values within the slots and thresholding these average values.
- Structure mating. This involves erosion using a SE shaped like a robot gripper. This gives possible gripper points. The stability of each possible gripping point (with respect to some direction) is also estimated.

[7] Crimmins, T.R.; Brown, W.M., "Image Algebra and Automatic Shape Recognition," *IEEE Trans. on Aerospace and Electronic Systems*, Vol. **AES-21**, pp. 60-69, Jan., 1985.

The authors present a shape-recognition transform, a special case of the hit-or-miss transformation. The key result is as follows: the shape T1 in window W occurs in the image I only at the locations $I \circledast (T1, W/T1)$. Also, the implementation of erosion as a standard convolution (under certain circumstances) is noted.

[8] Darwish, A.M.; Jain, A.K., "A Rule Based System for Automated Industrial Inspection," *SPIE Applications of Artificial Intelligence III*, Vol. **635**, pp. 172-81, 1986.

MM is used for defect detection on printed circuit boards. Defects include broken circuit paths, solder bridges, and missing pads.

[9] Destival, I.; Le Men, H., "Detection of Linear Networks on Satellite Images," *IEEE 8th Int. Conf. on Pattern Recognition*, Paris, France, pp. 856-58, 1986.

[10] Digabel, H., et. al "Etude de la distribution spatiale des ovogonies dans l'ovaire d'embryon de ratte à l'aide de l'analyseur de textures," *Annales de Biologie Animale*, Vol. **13**, pp. 115-125, 1973.

[11] Esselman, T.R.; Verly, J.G., "Some Applications of Mathematical Morphology to Range Imagery," *IEEE Proc. ICASSP-87*, Dallas, Tx., pp. 245-248, Vol. **1**, 1987.

This is a brief summary of the noise removal and 2-D feature extraction algorithms presented in this thesis.

[12] Hollingum, J., "The Shape of Things to Come," *Sensor Review* (GB), Vol. **6**, pp. 19-25, Jan., 1986.

This paper describes an automatic painted-surface inspection system. With the aid of specialized lighting, defects in painted surfaces appear in images as intensity changes. The size and shape of these defects can then be automatically analyzed through MM operations such as the rolling ball transformation and the opening.

[13] Holmes, Q.A.; Nüesch, D.R.; Shuchman, R.A., "Textural Analysis and Real-Time Classification of Sea-Ice Types Using Digital SAR Data," *IEEE Trans. Geosci. Rem. Sens.*, Vol. **GE-22**, No. 2, pp. 113-20, March, 1984.

Dilation and erosion using circular flat-top SEs are used for removing speckle noise from synthetic aperture radar data.

[14] Jeulin, D., "Morphological Quantitative Analysis of Multiphase Materials," *Mem. et Etud. Sci. Rev. Metall.* (France), Vol. **80**, No. 5, pp. 251-66, May, 1983 (in French).

The physical properties of multiphase materials, such as those encountered in metallurgy (e.g., iron ores), depend upon those of the individual phases, as well on the geometry and spatial organization of these phases. MM algorithms for noise removal, phase segmentation, and grain/pore size analysis are described and used in an automated system consisting of a scanning electron microscope and a Leitz texture analyzer.

[15] Lantuéjoul, Ch.; Serra, J., "M-Filters," *IEEE Proc. ICASSP-82*, Paris, pp. 2063-6, 1982.

Several new theoretical results are presented concerning morphological filters which are increasing and idempotent (M-Filters),[1] such as the opening and closing. The authors show that the union and intersection of increasing, idempotent operations is not in general increasing, and idempotent. Also, they show that an M-filtering has no effect if it is performed after a more powerful one. An example of M-filtering is given (from astronomy).

[16] Laÿ, B.; Baudoin, C.; Klein, J.C., "Automatic Detection of Microaneurysms in Retinopathy Fluoro-angiogram," *Proc. SPIE Int. Soc. Opt. Eng.*, Vol. **432**, pp. 165-73, 1983.

A magnified, gray-scale image of a fluoro-angiogram is searched for microaneurysms, which are specified according to their geometric properties. The algorithm begins with the rolling ball transform of the original image. This highlights blood vessels and microaneurysms. Then this transformed image is thresholded at several levels to produce binary images. These binary images contain "real" microaneurysms, noise made of small particles, and small blood vessels with diameter less than or equal to that of the microaneurysms. Locating the microaneurysms involves: 1) opening to remove small particles and 2) a sequence of hit-or-miss transformations to locate particles of the proper diameter for classification as microaneurysms. The algorithm is run on a Leitz Texture Analysis System (T.A.S.).

[17] Lee, J.S.J., "Morphologic Edge Detection," *IEEE 8th Int. Conf. on Pattern Recognition*, Paris, France, pp. 369-73, 1986.

---

[1] A transformation Ψ is increasing if $f \leq g \rightarrow \Psi(f) \leq \Psi(g)$, and idempotent if $\Psi[\Psi(f)] = \Psi(f)$.

Edge detection using MM is explored and a "minimum blur" edge detector is presented.

[18] Lee, Y.H., "Algorithms for Mathematical Morphological Operations with Flat Top Structuring Elements," *SPIE Applications of Digital Image Processing VIII*, Vol. **575**, pp. 33-45, 1985.

An iterative method of implementing erosion and dilation with flat-top SEs is presented. This method involves image shifting and comparisons (min and max) and would be suitable for a parallel array processor.

[19] Lougheed, R.M.; Tomko, L.M., "Robot Guidance Using a Morphological Vision Algorithm," *SPIE Intelligent Robots and Computer Vision*, Vol. **579**, pp. 367-76, 1985.

MM is used for bin picking. Several automotive parts are categorized according to uniques features such as orienting tabs and holes. The vision system employs MM running on a Cytocomputer for the detection of these features, and also for defect detection. A detailed example of a tab-finder is described.

[20] Mandeville, J.R., "Morphic Analysis of Printed Circuit Images," Research Report, IBM Watson Research Lab – Manufacturing Research Center, in *Opt. Soc. America, Topical Meeting on Machine Vision*, FD2/1-4, 1985.

Thinning is used to produce skeletons of printed circuit patterns. Then the hit-or-miss transformation is used to detect certain features of the skeleton. These features can be matched against a design feature list for fault detection.

[21] Maragos, P.A., *A Unified Theory of Translation-Invariant Systems with Applications to Morphological Analysis and Coding of Images*, Ph. D. Thesis, Georgia Inst. of Tech., July, 1985.

A relatively complete introduction to MM is presented along with new theoretical results. Application of the theoretical results to image coding is also presented. The key concepts and results:

- Maragos notes the distinction between *set-processing* systems and *function-processing* systems and the kernel representation of each.
- Extension of Matheron's work: any translation-invariant, increasing function-processing system can be realized as a supremum of erosions by all its kernel elements.
- If the system is also upper semi-continuous then a minimal set of kernel elements exists and is called the *basis* of the system. This basis may or may not be finite.

- The idea of a "pattern spectrum" is introduced as a means for shape analysis.

[22] Maragos, P.A.; Schafer, R.W., "Applications of Morphological Filtering to Image Analysis and Processing," *IEEE Proc. ICASSP-86*, Tokyo, Japan, pp. 2067-70, 1986.

This paper summarizes some applications of MM operations for edge detection, cleaning of impulsive noise, median filtering, skeletonization, and 2-D shape recognition.

[23] Maragos, P.A.; Schafer, R.W., "A Unification of Linear, Median, Order-Statistics and Morphological Filters Under Mathematical Morphology," *IEEE Proc. ICASSP-85*, Tampa, Fla., pp. 1329-32, 1985.

Maragos summarizes some of the theoretical results (listed above) obtained in his thesis.

[24] Maragos, P.A., "Pattern Spectrum of Images and Morphological Shape-Size Complexity," *IEEE Proc. ICASSP-87*, Dallas, Tx., pp. 241-244, Vol. 1, 1987.

A method of quantifying image structures through the opening and closing is presented. The method is based on taking the differences between consecutive openings or closings by SEs of various shapes and sizes.

[25] Maragos, P.A.; Schafer, R.W., "Morphological Skeleton Representation and Coding of Binary Images," *IEEE Proc. ICASSP-84*, San Diego, Ca., pp. 29.2.1-4, 1984.

This paper presents some of Maragos' preliminary work on image coding using MM.

[26] Matheron, G., *Random Sets and Integral Geometry*, Wiley, 1975.

Matheron develops the mathematical foundations of MM. This work is geared for the reader who wants to know more about the mathematical details of MM, as opposed to the more practical approach taken by Serra.

[27] Meyer, F., "Empiricism or Idealism," *Pattern Recognition in Practice: Proceedings of an International Workshop*, pp. 21-33, Publ. North-Holland, May, 1980.

Meyer discusses the differing philosophies of the "direct-measure" (empiricism) and "modify-then-measure" (idealism) approaches to image analysis. MM is traditionally used in "modify-then-measure" approaches and Meyer illustrates this in an example of cell culture analysis.

[28] Meyer, F., "Iterative Image Transformations for an Automatic Screening of Cervical Smears," *J. of Histochemistry and Cytochemistry*, Vol. **27**, No. 1, pp. 128-135, 1979.

This paper covers the early work of Meyer on biological cell analysis. The *top-hat transform* is introduced for detecting cells which appear as peaks in a gray-scale video image. Also, the conditional bisector and homotopic thinning are used to produce line drawings of cells. Pixel patterns in these line drawings are indicative of artifacts or defective cells. The work demonstrates the capability of an MM sequence to act as a "sieve" in analyzing images. This "sifting" approach is an efficient method of processing images since the MM sequences can be computed in parallel.

[29] Meyer, F., "Automatic Screening of Cytological Specimens," *CVGIP*, Vol. **35**, pp. 356-369, 1986.

This paper is similar to the above paper, except that improvements and new techniques are discussed. A MM edge detector and the top-hat transform (to eliminate artifacts) are used to focus the microscope images. Also, background normalization is accomplished through the rolling ball transform.

[30] Nawrath, R.; Serra, J., "Quantitative Image Analysis: Theory and Instrumentation," *Microsc. Acta* (Germany), Vol. **82**, No. 2, pp. 101-11, Sept., 1979.

This paper includes notes on upgrades of the Leitz T.A.S. as well as gradient detection and contour extraction algorithms. The gradient detection algorithm involves MM operations on slices of a gray-scale function.

[31] Nawrath, R.; Serra, J., "Quantitative Image Analysis: Applications Using Sequential Transformations," *Microsc. Acta* (Germany), Vol. **82**, No. 2, pp. 113-28, Sept., 1979.

Several applications of MM are presented in this paper. These applications include: (1) rectangular fiber analysis, (2) separation of clustered cells, and (3) the computation of the number of edges of polygonal cells in a tessalation (a tessalation is an aggregate of non-overlapping cells which cover an image).

[32] Peters, R.A.; Strickland, R., "Image Analysis Using Hit-or-miss Transforms with Resolution Pyramids," *SPIE Applications of Digital Image Processing IX*, Vol. **697**, pp. 197-209, 1986.

[33] Rodenacker, K.; Gais, P.; Jütting, U.; Burger, G., "Mathematical Morphology in Grey-Images," *Signal Processing II: Theories and Applications, Proc. EUSIPCO-83*, Erlangen, Germany, pp. 131-4, Publ. North-Holland, Sept.,

1983.

MM is applied to the analysis of human cell images. The *rice field transformation*, which can provide a reasonably tractable description of the topology of an image, is introduced.

[34] Serra, J., *Image Analysis and Mathematical Morphology*, Acad. Press, 1982.

A complete description of MM is given along with many practical algorithms for image analysis. The information in this reference can be considered the state of the art of MM (up to 1982).

[35] Serra, J., "Principles, Criteria and Algorithms in Mathematical Morphology," *Issues in Digital Image Processing: Proc. NATO Advanced Study Inst. on Dig. Image Processing and Analysis*, pp. 73-105, 1980.

The first part of this paper is quite similar to material in Serra's book. It highlights the important mathematical characteristics of MM such as invariance under translation, compatibility with magnification, local knowledge, and semi-continuity. The second part of this paper covers two examples of MM analysis: wood textures analyzed by variograms; size distributions of porous media analyzed by morphological openings.

[36] Serra, J., "Quantitative Image Analysis," *Recherche* (France), Vol. **9**, No. 87, pp. 247-56, March, 1978 (in French).

This is an introduction to image analysis and automatic image analysers. The author emphasizes the principle of image transformation followed by measurements. These principles were first used in the early 60s by the english "Quantimets" and then from the late 60s by the french-german "Texture Analysers". These systems are based on classical integral geometry and on MM, respectively. Texture analysers are used (as of 1978) as follows: 50% for material science, 40% for biology, and 10% for macroscopic imagery (e.g., aerial photographs). The wide range of applications is illustrated through two extreme examples, i.e., recognition of cells and structural analysis of woods. Other application areas are cited.

[37] Serra, J., "Introduction to Mathematical Morphology," *CVGIP*, Vol. **35**, pp. 283-305, 1986.

This paper serves as a tutorial and overview of MM. It serves as an excellent supplement to Serra's book.

[38] Shapiro, L.G.; MacDonald, R.S.; Sternberg, S.R., "Shape Recognition with Mathematical Morphology," *IEEE 8th Int. Conf. on Pattern Recognition*, Paris, France, pp. 416-18, 1986.

MM is used to decompose binary image shapes into primitives. These primitives are used in a polynomial-time matching algorithm for object recognition.

[39] Skolnick, M.M., "Application of Morphological Transformations to the Analysis of Two-Dimensional Electrophoretic Gels of Biological Materials," *CVGIP*, Vol. **35**, pp. 306-332, 1986.

[40] Sternberg, S.R., "Biomedical Image Processing," *IEEE Computer*, Vol. **16**, No. 1, pp. 22-34, Jan., 1983.

This gives an excellent description of 2-D and 3-D MM, although the notation is not identical to that of Serra's. This biomedical application of MM involves the search for mutations in cell images using a Cytocomputer. The Cytocomputer architecture is described as are MM methods for background normalization, streak removal, and cell isolation.

[41] Sternberg, S.R., "Industrial Morphology," *SPIE Applications of Digital Image Processing VIII*, Vol. **504**, pp. 202-13, 1984.

The author demonstrates the capabilities of MM for 2-D pattern recognition. The MM opening aids in the discrimination of several polygons such as rectangles and triangles. The examples shown provide a good illustration of the potential of MM for 2-D pattern recognition.

[42] Sternberg, S.R.; Sternberg, E., "Industrial Inspection by Morphological Virtual Gauging," *Proc. IEEE Computer Society Workshop on Computer Architecture for Pattern Analysis and Image Database Management*, pp. 237-47, Oct., 1983.

A simple MM algorithm for the detection of defects in watch gears is described. The hardware and software of the MVI (Machine Vision International) machine vision system are also described.

[43] Sternberg, S.R., "Grayscale Morphology," *CVGIP*, Vol. **35**, pp. 333-355, 1986.

[44] Watson, G.S., "Mathematical Morphology," Tech. Rept., Princeton Univ. Dept. of Statistics, TR-21-SER-2, March, 1973.

This paper is a relatively short summary of MM theory. The author provides concise and accurate descriptions of the basic MM operations, along with an intuitive introduction to some of the more advanced theory. The mathematical

vocabulary and style of presentation are somewhat more accessible to the non-specialist, thus, this paper would serve as an excellent supplement to Serra's book.

[45] Watson, G.S., "Mathematical Morphology," *A Survey of Statistical Design and Linear Models*, ed. J.N. Srivastava, pp. 547-53, North-Holland, 1975.

This is a condensed version of the above paper.

[46] Zhuang, Z.; Haralick, R.M., "Morphological Structuring Element Decomposition," *CVGIP*, Vol. **35**, pp. 370-382, 1986.

In this paper, the theory of optimal SE decomposition is explored. A tree search algorithm for SE decomposition is given.

Architectures

[47] Dobaj, A.P., "System Architecture of a SIMD Image Processor Optimized for Morphologic Processing," *Proc. Topical Meeting on Machine Vision*, Incline Village, Nevada, March 18-20, 1987.

This is a brief paper on the PMIP – a 256-processor, SIMD image processor. Among the topics discussed are: host interface, video I/O, processor architecture, feature extraction hardware, and programming environment.

[48] Klein, J.C., "The Texture Analyzer," *J. Microsc.*, Vol. **92**, Pt. 2, pp. 349-356, April, 1972.

This is a description of one of the first MM computers, the Texture Analyzer. It operates on binary images which are contained in serially connected shift registers (a delay line). The shift registers are tapped at appropriate places in the delay line to provide a 2-D window on the data. This window is used in computing the programmed transformation. The fundamental operation supported by the Texture Analyzer is the hit-or-miss transformation.

[49] Kosykh, V.P., "Software Implementation of a Morphological Processor," *Autometriya* (USSR), Trans. in *Autom. and Monit. and Measures* (GB), No. 4, pp. 75-78, 1982.

A relatively simple software model of a parallel MM processsor is described. The model uses a 128 × 128 hexagonal grid and the hit-or-miss transformation as its basic operation. The architecture can be used for binary and gray-scale processing.

[50] Lougheed, R.M.; McCubbrey, D.L., "The Cytocomputer: A Practical Pipelined Image Processor," *Proc. 7th Ann. Int. Symp. on Comp. Arch.*, pp. 271-77, May, 1980.

The Cytocomputer employs a chain of serial neighborhood-processing stages which are similar to that of the Texture Analyzer. Window access to the image data is accomplished by tapping the serial image data at the proper locations so that both point and neighborhood transformations are possible. The Cytocomputer allows binary and limited gray-scale processing (a $3 \times 3 \times 3$ array is the maximum-size SE). Performance of the Cytocomputer is compared to that of array processors.

[51] Nawrath, R., "The LEITZ T.A.S., new possibilities of image analysis," *LEITZ Sci. and Tech. Inf.* (Germany), Vol. **7**, No. 6, pp. 168-173, June, 1979.

The overall organization of the T.A.S. is presented; no specific hardware design is discussed. The focus is on the new additions to the T.A.S. which include new hardware units as well as integration of a minicomputer. These additions enable users to modify images interactively.

[52] Pecht, J., "Speeding up successive Minkowski operations with bit-plane computers," *Pattern Recognition Letters*, Vol. **3**, pp. 113-117, March, 1985.

A new set MM theory on the decomposition of SEs of the form $nB = B \oplus B \oplus B \ldots$ is presented. It is shown that after a certain number of steps in the expansion of nB, only the "extreme points" of the the SE B are important.

[53] Preston, K. Jr., "Cellular Logic Arrays for Image Processing," *Handbook of Pattern Recognition and Image Processing*, pp. 395-436, Acad. Press, 1986.

This is an excellent introduction to cellular logic architectures. Though not specifically designed for MM, most of the architectures can support a wide range of MM computations. The architectures described include:

- CELLSCAN
- GLOPR (Golay LOgic PRocessor)
- BIP (Binary Image Processor)
- ILLIAC IV
- diff3
- Cytocomputer
- PHP (Preston-Herron Processor)

- PICAP (PICture Array Processor)
- DIP (Delft Array Processor)
- CLIP (Cellular Logic Image Processor)
- MPP (Massively Parallel Processor)

Information such as the number of processing elements, image size, processing rate, host computer, etc., is provided for each of the architectures. The author also describes several cellular array programming languages such as GLOL, C3PL, PPL, CAP4, and DAP-FORTRAN.

[54] Preston, K. Jr.; Duff, M.J.B.; Levialdi, S.; Norgren, P.E.; Toriwaki J., "Basics of Cellular Logic with Some Applications in Medical Image Processing," *Proc. IEEE*, Vol. **67**, No. 5, pp. 826-56, May, 1979.

This paper covers the history, theoretical background, and fundamental operation sequences of cellular logic computers. Blood cell image analysis and biopsy tissue analysis are given as example applications.

[55] Sternberg, S.R., "Computer Architectures Specialized for Mathematical Morphology," *Algorithmically Specialized Parallel Computers*, ed. L. Snyder, L.H. Jamieson, D.B. Gannon, and H.J. Siegel, Acad. Press, 1985.

The title of this paper is misleading: the primary topic is the Cytocomputer (see Lougheed above). To overcome some of the inherent limitations of the Cytocomputer (a single serial processor), the author proposes the use of several serial processors running in parallel.

[56] Sternberg, S.R., "Morphological Cellular Logic Image Processor Architectures," *SPIE*, Vol. **435**, pp. 112-120, Aug., 1983.

A MM tutorial is given along with a description of the Cytocomputer (see above).

[57] Sternberg, S.R., "Language and Architecture for Parallel Image Processing," *Pattern Recognition in Practice*, E.S. Gelsema and L.N. Kanal (eds.), pp. 35-44, North-Holland, 1980.

This paper covers the Cytocomputer and its command language C3PL. The computation of the medial axis transform is given as an example.

[58] Sternberg, S.R., "Parallel Architectures for Image Processing," *Proc. IEEE COMPSAC*, pp. 712-717, 1979.

The author discusses the basic MM operations and their relation to hardware

design. He notes that MM operations are amenable to parallel array implementation but that this type of architecture can be very costly. As a solution, Sternberg proposes a pipelined architecture (the Cytocomputer).

[59] Sternberg, S.R., "Parallel Processing in Machine Vision," *Proc. Robotic Intelligence and Productivity Conf.*, pp. 35-44, 1983.

This paper discusses improvements to the Cytocomputer architecture which resulted in the Genesis 2000 machine vision system. The improvements come from specialization of hardware. The hardware specializations include: an arithmetic logic unit (add, subtract, multiply, divide, and logically compare images); a geometric logic unit (basic MM operations); a count and locate unit (count the number of pixels satisfying a certain condition); a central processing unit (to control the other hardware units and peripheral devices).

Related

[60] Blum, H., "Biological Shape and Visual Science (Part 1)," *J. Theoretical Biology*, Vol. **38**, pp. 205-287, 1973.

[61] Blum, H., "A Transformation for Extracting New Descriptors of Shape," *Proc. Symp. on Models for Perception of Speech and Visual Form*, W. Whaten-Dunn (ed.), MIT Press, Cambridge, Ma., 1967.

[62] Golay, M.J.E., "Hexagonal Parallel Pattern Transformation," *IEEE Trans. Comp.*, Vol. **C-18**, pp. 733-40, 1969.

[63] Levialdi, S., "Parallel Pattern Processing," *IEEE Trans. Syst. Man and Cybern.*, *SMC-1*, pp. 292-296, 1971.

[64] Ronse, C., "Erosion of Narrow Image Features by Combination of Local Low Rank and Max Filters," *Proc. 2nd Int. Conf. on Image Proc. and its Applications*, pp. 77-81, June, 1986.

This author discusses mathematical properties of min and max filters. The notation is entirely different from Serra's.

[65] Serra, J., "Descriptors of Flatness and Roughness," *J. Microsc.* (GB), Vol. **134**, Pt. 3, pp. 227-43, June, 1984.

This is a highly mathematical discussion of the concepts of flatness and roughness. The paper contains minimal information on MM although it describes

flatness and roughness measurements which could be performed using MM. The flatness and roughness of road surfaces and typographical fonts are analyzed.

[66] Wendt, P.D.; Coyle, E.J.; Gallagher, N.C. Jr., "Stack Filters," *IEEE Trans. Acoustics, Speech, and Signal Processing*, Vol. **ASSP-34**, No. 4, pp. 898-911, Aug., 1986.

The authors discuss implementation of filters which obey a threshold decomposition law (such as M-filters with flat-top SEs). Though not specifically designed for MM, this implementation appears to be reasonably efficient for the case of a flat-top SE.

[67] Werman, M.; Peleg, S., "Min-Max Operators in Texture Analysis," *IEEE Trans. Pattern Anal. Mach. Int.*, Vol. **PAMI-7**, No. 6, pp. 730-733, Nov., 1985.

Miscellaneous

[68] Hua, H.Z.; Qian, Y., "A Direct Corner Detecting Algorithm," *IEEE 8th Int. Conf. on Pattern Recognition*, Paris, France, pp. 853-55, 1986.

[69] J.G. Verly; P.L. Van Hove; R.L. Walton, D.E. Dudgeon, "Silhouette Understanding System," *Proc. ICASSP-86*, pp. 1457-1460, 1986.

[70] Winston, P.H.; Horn, B.K.P.; *LISP*, Addison-Wesley, 1981.

[71] Zuniga, O.A.; Haralick, R., "Corner Detection Using the Facet Model," *IEEE CVPR Conf*, pp. 30-37, 1983.

REPORT DOCUMENTATION PAGE

1a. REPORT SECURITY CLASSIFICATION	1b. RESTRICTIVE MARKINGS
Unclassified	

2a. SECURITY CLASSIFICATION AUTHORITY	3. DISTRIBUTION/AVAILABILITY OF REPORT
2b. DECLASSIFICATION/DOWNGRADING SCHEDULE	Approved for public release; distribution unlimited.

4. PERFORMING ORGANIZATION REPORT NUMBER(S)	5. MONITORING ORGANIZATION REPORT NUMBER(S)
Technical Report 797	ESD-TR-87-244

6a. NAME OF PERFORMING ORGANIZATION	6b. OFFICE SYMBOL (If applicable)	7a. NAME OF MONITORING ORGANIZATION
Lincoln Laboratory, MIT		Electronic Systems Division

6c. ADDRESS (City, State, and Zip Code)	7b. ADDRESS (City, State, and Zip Code)
P.O. Box 73 Lexington, MA 02173-0073	Hanscom AFB, MA 01731

8a. NAME OF FUNDING/SPONSORING ORGANIZATION	8b. OFFICE SYMBOL (If applicable)	9. PROCUREMENT INSTRUMENT IDENTIFICATION NUMBER
Defense Advanced Research Projects Agency	TTO	F19628-85-C-0002

8c. ADDRESS (City, State, and Zip Code)	10. SOURCE OF FUNDING NUMBERS			
	PROGRAM ELEMENT NO.	PROJECT NO.	TASK NO.	WORK UNIT ACCESSION NO.
1400 Wilson Boulevard Arlington, VA 22209	62702E	306		

11. TITLE (Include Security Classification)

Applications of Mathematical Morphology to Range Imagery

12. PERSONAL AUTHOR(S)
Thomas R. Esselman and Jacques G. Verly

13a. TYPE OF REPORT	13b. TIME COVERED	14. DATE OF REPORT (Year, Month, Day)	15. PAGE COUNT
Technical Report	FROM _____ TO _____	1987 December 23	80

16. SUPPLEMENTARY NOTATION

None

17. COSATI CODES			18. SUBJECT TERMS (Continue on reverse if necessary and identify by block number)
FIELD	GROUP	SUB-GROUP	mathematical morphology computer vision
			range imagery image processing
			feature extraction

19. ABSTRACT (Continue on reverse if necessary and identify by block number)

Although little known, mathematical morphology offers great potential in the areas of image enhancement, feature extraction, and object recognition. This work explores this growing field through a survey of established morphological algorithms and the development of new morphological algorithms for range image analysis. With range imagery, mathematical morphology is used for noise removal, 2-D feature extraction, 3-D feature extraction, and 3-D corner extraction.

20. DISTRIBUTION/AVAILABILITY OF ABSTRACT	21. ABSTRACT SECURITY CLASSIFICATION
☐ UNCLASSIFIED/UNLIMITED ☒ SAME AS RPT. ☐ DTIC USERS	Unclassified

22a. NAME OF RESPONSIBLE INDIVIDUAL	22b. TELEPHONE (Include Area Code)	22c. OFFICE SYMBOL
Lt. Col. Hugh L. Southall, USAF	(617) 981-2330	ESD/TML

DD FORM 1473, 84 MAR   83 APR edition may be used until exhausted.   UNCLASSIFIED
All other editions are obsolete.